Diversity of Kilonova Light Curves

Kyohei Kawaguchi[1,2], Masaru Shibata[2,3] , and Masaomi Tanaka[4]

[1] Institute for Cosmic Ray Research, The University of Tokyo, 5-1-5 Kashiwanoha, Kashiwa, Chiba 277-8582, Japan
[2] Center for Gravitational Physics, Yukawa Institute for Theoretical Physics, Kyoto University, Kyoto 606-8502, Japan
[3] Max Planck Institute for Gravitational Physics (Albert Einstein Institute), Am Mühlenberg 1, Potsdam-Golm D-14476, Germany
[4] Astronomical Institute, Tohoku University, Aoba, Sendai 980-8578, Japan

Abstract

We perform radiative transfer simulations for kilonova in various situations, including the cases of prompt collapse to a black hole from neutron star mergers, high-velocity ejecta possibly accelerated by magnetars, and a black hole–neutron star merger. Our calculations are done employing ejecta profiles predicted by numerical-relativity simulations and a new line list for all the *r*-process elements. We found that: (i) the optical emission for binary neutron stars promptly collapsing to a black hole would be fainter by $\gtrsim$1–2 mag than that found in GW170817, while the infrared emission could be as bright as that in GW170817 if the post-merger ejecta is as massive as $\approx 0.01\,M_\odot$; (ii) the kilonova would be brighter than that observed in GW170817 for the case that the ejecta is highly accelerated by the electromagnetic energy injection from the remnant, but within a few days it would decline rapidly and the magnitude would become fainter than in GW170817; and (iii) the optical emission from a black hole–neutron star merger ejecta could be as bright as that observed in GW170817 for the case that sufficiently large amount of matter is ejected ($\gtrsim 0.02\,M_\odot$), while the infrared brightness would be brighter by 1–2 mag at the same time. We show that the difference in the ejecta properties would be imprinted in the differences in the peak brightness and time of peak. This indicates that we may be able to infer the type of the central engine for kilonovae by observation of the peak in the multiple band.

1. Introduction

The simultaneous detection of gravitational waves (GWs) from a neutron star–neutron star (NS–NS) merger (Abbott et al. 2017b) and its electromagnetic (EM) counterparts opened a new window of multi-messenger astronomy. EM counterparts to GW170817 have been observed over the entire wavelength range, from gamma-ray to radio wavelengths (Abbott et al. 2017a; Andreoni et al. 2017; Arcavi et al. 2017; Coulter et al. 2017; Cowperthwaite et al. 2017; Díaz et al. 2017; Drout et al. 2017; Evans et al. 2017; Hallinan et al. 2017; Hu et al. 2017; Valenti et al. 2017; Kasliwal et al. 2017; Lipunov et al. 2017; Pian et al. 2017; Smartt et al. 2017; Tanvir et al. 2017; Troja et al. 2017; Utsumi et al. 2017; Mooley et al. 2018; Pozanenko et al. 2018). In particular, a counterpart in optical and infrared wavelengths (named as SSS17a, AT 2017gfo or DLT17ck) has been identified as the emission of a so-called a kilonova (also known as macronova).

A kilonova is the emission that has been expected to be associated with NS mergers as a consequence of the mass ejection from the system (e.g., Rosswog et al. 1999; Ruffert et al. 2001; Hotokezaka et al. 2013). Since the ejected material is composed of neutron-rich matter, heavy radioactive nuclei can be synthesized in the ejecta by the so-called *r*-process nucleosynthesis (Lattimer & Schramm 1974; Eichler et al. 1989; Korobkin et al. 2012; Wanajo et al. 2014). In addition, EM emission in the optical and infrared wavelengths can be powered by radioactive decays of heavy elements (Li & Paczynski 1998; Kulkarni 2005; Metzger et al. 2010; Kasen et al. 2013; Tanaka & Hotokezaka 2013). Previous studies (Li & Paczynski 1998; Kasen et al. 2013, 2015; Barnes et al. 2016; Wollaeger et al. 2018; Tanaka et al. 2017, 2018) show that the light curves of kilonovae depend on the mass, velocity, and

opacity of ejecta. The peak luminosity and the time at the peak luminosity are approximately estimated as

$$L_{\rm peak} \approx 1.3 \times 10^{42}\ {\rm erg\ s^{-1}} \left(\frac{f}{10^{-6}}\right)\left(\frac{M}{0.03\,M_\odot}\right)^{1/2}$$
$$\times \left(\frac{v}{0.2c}\right)^{1/2}\left(\frac{\kappa}{1\ {\rm cm^2\ g^{-1}}}\right)^{-1/2} \tag{1}$$

and

$$t_{\rm peak} \approx 4.9\ {\rm days}$$
$$\times \left(\frac{M}{0.03\,M_\odot}\right)^{1/2}\left(\frac{v}{0.2c}\right)^{-1/2}\left(\frac{\kappa}{1\ {\rm cm^2\ g^{-1}}}\right)^{1/2}, \tag{2}$$

where M, v, κ, f, and c are the ejecta mass, velocity, opacity, heating efficiency with respect to the restmass energy (see Li & Paczynski 1998 for the detail), and the speed of light, respectively. Previous studies (Kasen et al. 2013; Tanaka & Hotokezaka 2013; Kasen et al. 2015; Barnes et al. 2016; Tanaka et al. 2017, 2018; Wollaeger et al. 2018) have shown that the opacity of ejecta varies significantly ($\kappa = 0.1$–10 cm^2 g^{-1}) depending on the electron fraction of the ejecta (Y_e, number of protons per nucleon, which controls the final element abundances). Thus, to predict the kilonova light curves, it is crucial to understand the properties of the ejecta (e.g., the mass, density distribution, and composition).

The properties of the ejecta depend on the masses (and spins) of the binary components, the NS equation of state, and the mass ejection mechanism. In particular, the ejecta properties reflect the fate of the system after the merger. Thus, the

kilonova light curves will carry the physical information of the merged binary and the post-merger evolution of the system as complementary information to that inferred by the GW data analysis. For example, a number of studies have shown that the optical and infrared EM counterparts to GW170817 are consistent with kilonova models composed of multiple components (e.g., Cowperthwaite et al. 2017; Kasen et al. 2017; Kasliwal et al. 2017; Villar et al. 2017; Kawaguchi et al. 2018), which suggests that a substantial fraction is likely to be lanthanide-free. The presence of lanthanide-free ejecta indicates that the remnant NS temporarily survived before it eventually collapsed to a black hole (BH).

While detailed observational data obtained for the kilonova associated with GW170817 would be a standard guideline, the following events would not always be similar to the previous event. As we discuss in the next section, kilonova light curves could show a large diversity, which reflects the variety in the ejecta properties that depend on the binary parameters or the binary composition. Indeed, the diversity of kilonova light curves has been suggested in previous studies of the kilonova candidates found in the archive observational data of short gamma-ray-burst afterglows (Gompertz et al. 2018; Ascenzi et al. 2019; Rossi et al. 2019). Thus, in this work, we perform radiative transfer simulations for kilonova light curves in various situations predicted by numerical-relativity simulations to investigate their possible diversity. In our previous study (Kawaguchi et al. 2018), we performed an axisymmetric radiative transfer simulation for kilonovae while taking the radiative transfer effect of photons in the multiple ejecta components of non-spherical morphology into account, and we demonstrated that this photon transfer effect could have a large impact on predicting the light curves. In this paper, we will show the roles that this effect plays by performing the calculations for a variety of ejecta models.

This paper is organized as follows. In Section 2, we briefly summarize the variety in the ejecta properties predicted by recent numerical simulations. In Section 3, we describe our method for radiative transfer simulations and the setups for ejecta profile, and we summarize the models that we study in this paper. In Section 4, we study how large the impact of the radiative transfer effect of photons in the multiple ejecta components to the light curve predictions could be, and we show the dependence of the light curves on the ejecta parameters. An interpretation of the optical and infrared EM counterparts to GW170817 based on our new calculation is also discussed in Section 5. In Section 6, we show a variety of NS merger models, such as the cases of prompt collapse to a BH from NS mergers, high-velocity ejecta possibly accelerated by magnetars, and a BH–neutron star (BH–NS) merger. We summarize our findings in Section 7. Throughout this paper, magnitudes are given in the AB magnitude system.

2. Variety in the Ejecta Properties

In this section, we will briefly summarize the variety in the ejecta properties predicted by numerical-relativity simulations for NS mergers. For the last decade, many numerical simulations for NS–NS mergers have been performed to investigate the properties of the ejected material. These studies reveal that there are broadly two types of mass ejection mechanisms. The first type is called dynamical mass ejection, which occurs within ∼10 ms after the onset of mergers. In this timescale, the NS material is ejected by the angular momentum transport via tidal force of the merger remnant or by the shock heating which takes place in the collisional surface of the NSs (Bauswein et al. 2013; Hotokezaka et al. 2013; Sekiguchi et al. 2015, 2016; Radice et al. 2016; Bovard et al. 2017; Dietrich et al. 2017). The second type is called post-merger ejection, which occurs in the timescale up to ∼0.1–10 s after the mergers. Post-merger ejecta is launched from the remnant of the merger, such as a system composed of a massive NS or BH with a massive torus, driven by amplified magnetic fields or effective viscous heating due to magnetic turbulence (Dessart et al. 2009; Metzger & Fernández 2014; Perego et al. 2014; Just et al. 2015; Lippuner et al. 2017; Shibata et al. 2017; Siegel & Metzger 2017; Fujibayashi et al. 2018).

Figure 1 summarizes the possible scenarios for the post-merger evolution and the typical properties of ejecta for a variety of NS mergers. For a NS–NS merger, the fate after the merger can be broadly categorized into three cases:

The first case is the prompt collapse to a BH. In this case the NSs collapse promptly to a BH (which are described as a prompt-collapse case in the following). For most of the prompt-collapse cases, both dynamical ejecta and remnant torus mass are suppressed, and are typically $\lesssim 0.001\,M_\odot$ and $\lesssim 0.01\,M_\odot$, respectively, unless the mass ratio is $\lesssim 0.8$ (Kiuchi et al. 2009; Hotokezaka et al. 2013). Due to the absence of neutrino radiation from the remnant, the electron fraction in the post-merger ejecta would remain low and consequently the ejecta would be lanthanide-rich for the prompt-collapse cases (Metzger & Fernández 2014; Wu et al. 2016; Lippuner et al. 2017; Siegel & Metzger 2017; Fernández et al. 2019).

The second case is a hypermassive massive neutron star (HMNS). In this case a HMNS is formed temporarily and the remnant collapses to a BH after surviving for more than 10 ms. The mass of the dynamical ejecta and the remnant torus can be massive, up to ∼0.001–0.01 $M_\odot$ and ∼0.1 $M_\odot$, respectively (Bauswein et al. 2013; Hotokezaka et al. 2013; Sekiguchi et al. 2015, 2016; Radice et al. 2016; Bovard et al. 2017; Dietrich et al. 2017). Y_e of the dynamical ejecta can be raised due to electron/positron capture and the neutrino irradiation from the remnant (Sekiguchi et al. 2015). The previous studies show that the dynamical ejecta in the polar region can be lanthanide-free, while that in the equatorial plane would remain to be lanthanide-rich. Y_e of the post-merger ejecta depends strongly on the lifetime of the remnant NS. The previous studies also show that post-merger ejecta would be lanthanide-free if the remnant NS is sufficiently long-surviving ($t_{\rm life} \gtrsim 1$ s, where $t_{\rm life}$ is the timescale for the remnant to collapse to a BH), while a substantial amount of lanthanide is synthesized if the remnant collapses to a BH in a short timescale (Metzger & Fernández 2014; Perego et al. 2014; Wu et al. 2016; Lippuner et al. 2017; Siegel & Metzger 2017; Fujibayashi et al. 2018; Fernández et al. 2019).

The third case is a long-lived super massive neutron star (SMNS). In this case the remnant NS survives for a long period ($t_{\rm life} \gg 1$s) or does not collapse to a BH. This situation can be realized if the total mass of the binary is close to or smaller than the maximum mass of a rigidly rotating NS (SMNS). For this case, the mass of the dynamical ejecta would be relatively small (order of $10^{-3}\,M_\odot$) unless the mass ratio of the binary is far from unity (Bauswein et al. 2013; Hotokezaka et al. 2013; Foucart et al. 2016; Radice et al. 2016; Bovard et al. 2017; Dietrich et al. 2017). In contrast, the post-merger ejecta could be massive (∼0.01–0.1 $M_\odot$), due to the large remnant torus
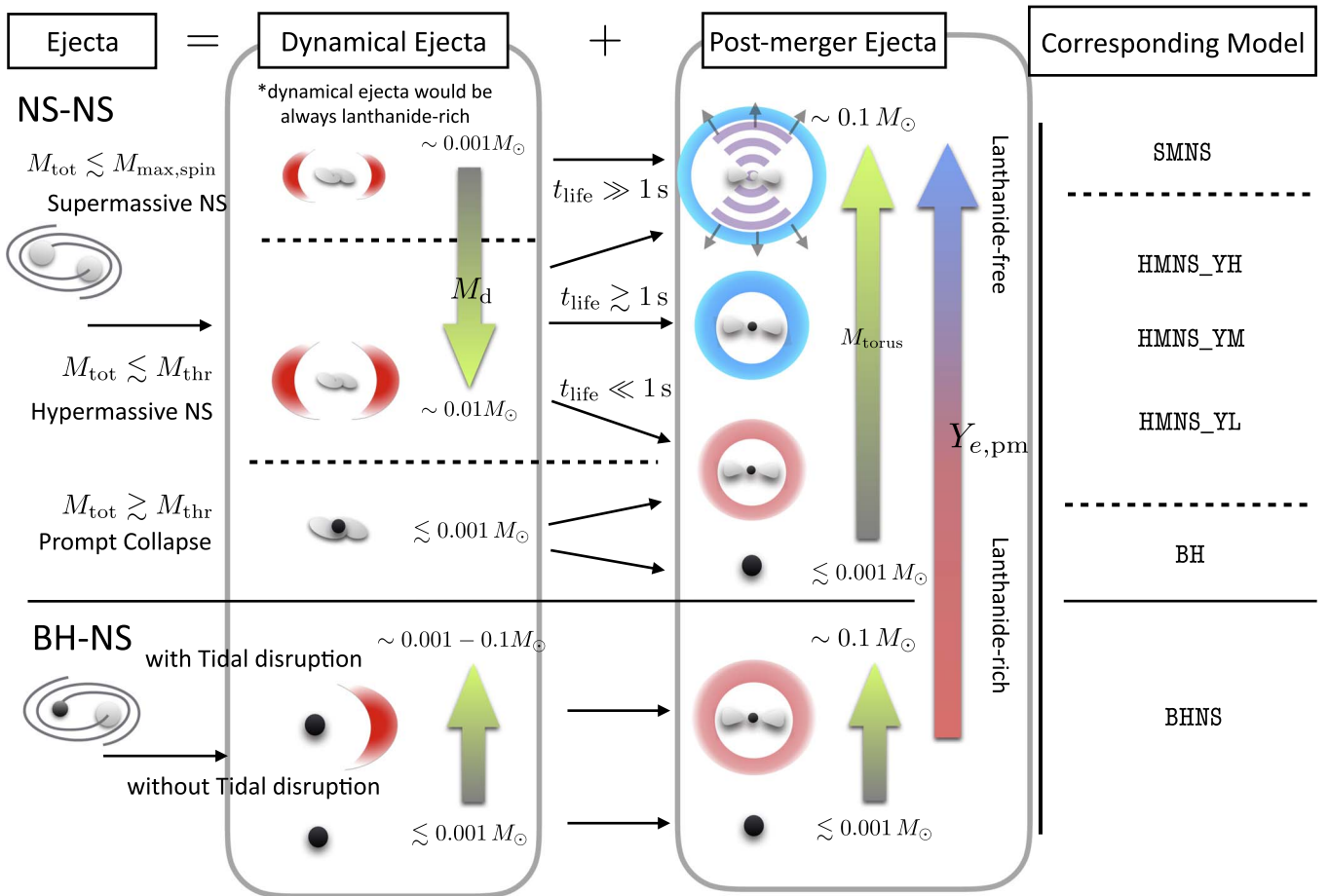
Figure 1. Schematic picture of the post-merger evolution and the typical properties of ejecta for NS–NS and BH–NS binaries in various situations. We note that our ejecta model consists of two parts: the dynamical ejecta with non-spherical geometry and the post-merger ejecta with spherical geometry. M_{tot}, $M_{max,spin}$, M_{thr}, M_d, M_{torus}, and t_{life} are the total mass of the binary, maximum mass of a rigidly rotating NS, threshold total mass for the prompt collapse, dynamical ejecta mass, remnant torus mass, and the timescale for the remnant to collapse to a BH, respectively. The correspondence between each situation and kilonova models listed in Table 1 is summarized on the right-hand side of the figure. We note that this figure only shows a simplified overview for the typical scenario. We also note that the quantitative properties of the post-merger evolution and mass ejection depend on the detail of the binary parameters, such as the mass ratio, spins, and equation of state of NS (see the references mentioned in the main text).

mass, and it would be lanthanide-free because of neutrino irradiation (Fujibayashi et al. 2018).

In addition, the rotational kinetic energy of the remnant NS could be an additional energy source to the ejecta by releasing it through the EM radiation, which could modify the light curves for the early phase $\lesssim 1$ days (Metzger & Piro 2014; Margalit & Metzger 2017; Shibata et al. 2017). We note that the efficiency and timescale for releasing the rotational kinetic energy of the remnant NS to the ejecta are currently quite uncertain. In particular, if the timescale of the energy injection is much shorter than the timescale of the kilonova emission, ~ 1–10 days, then the energy injected into the ejecta would be lost by adiabatic expansion and would not be directly reflected in the light curves. However, even for such a case, the light curves could show different feature from the case in the absence of the energy injection from the remnant because the ejecta profile would be modified by the increase in its kinetic energy. Indeed, the rotational kinetic energy of the NS could be as large as ≈ 1–2×10^{53} erg for the case of mass shedding limit (e.g., Margalit & Metzger 2017; Shibata et al. 2017, 2019) and it is sufficiently large to modify the velocity distribution of the ejecta, even if only a small fraction of the

rotational kinetic energy is converted to the kinetic energy of ejecta, which is typically $\sim 10^{49}$–10^{51} erg. In this work, for simplicity, we focus on the case where the activity of the remnant NS only contributes to changing the ejecta profile. There may also be a case where the remnant activity directly affects the light curves (Wollaeger et al. 2019).

A black hole–neutron star merger (BH–NS) can also be associated with the EM counterparts if the NS is tidally disrupted before the merger (Rosswog 2005; Shibata & Taniguchi 2008; Etienne et al. 2009; Lovelace et al. 2013; Kyutoku et al. 2015; Kawaguchi et al. 2016; Foucart et al. 2019, 2018). The masses of the dynamical ejecta and the remnant torus can be much more and/or less massive than those formed in a NS–NS merger. Their values depend strongly on the parameters of the binary, such as the NS radius, mass ratio of the BH to the NS, and particularly the BH spin. Because of the absence of the strong shock heating effect in the merger and post-merger processes, Y_e of the dynamical ejecta keeps the original value of the NS, $Y_e \lesssim 0.1$ (Rosswog et al. 2013; Just et al. 2015; Foucart et al. 2017; Kyutoku et al. 2018). Y_e of the remnant torus and that of the post-merger ejecta could raise due to viscous heating but a substantial

amount of the post-merger ejecta would be lanthanide-rich, as in the prompt collapse of NS–NS cases.

3. Method

3.1. Radiative Transfer Simulation

We calculate the light curves of kilonovae/macronovae by a wavelength-dependent radiative transfer simulation code (Tanaka & Hotokezaka 2013; Tanaka et al. 2017, 2018). The photon transfer is calculated by a Monte Carlo method for given ejecta profiles of density, velocity, and element abundance. The nuclear heating rates are determined by employing the results of r-process nucleosynthesis calculations by Wanajo et al. (2014). We also consider the time-dependent thermalization efficiency following an analytic formula derived by Barnes et al. (2016). Axisymmetry is imposed for the matter profile, such as the density, temperature, abundance distribution. Special-relativistic effects on photon transfer and light travel time effects are fully taken into account.

For photon-matter interaction, we consider the same physical processes as in Tanaka & Hotokezaka (2013), Tanaka et al. (2017, 2018); that is, bound–bound, bound–free, and free–free transitions and electron scattering for a transfer of optical and infrared photons. For the bound–bound transitions, which have a dominant contribution in the optical and infrared wavelengths, we use the formalism of the expansion opacity (Eastman & Pinto 1993; Kasen et al. 2006). For atomic data, the updated line list calculated in Tanaka et al. (2019) is employed. This line list is constructed by an atomic structure calculation for all the elements from $Z = 26$ to $Z = 92$, and supplemented by Kurucz's line list for $Z < 26$ (Kurucz & Bell 1995), where Z is the atomic number. The updated atomic data include up to triple ionization for all of the ions. The ionization and excitation states are calculated under the assumption of local thermodynamic equilibrium (LTE) by using the Saha ionization and Boltzmann excitation equations.

3.2. Ejecta Profile

In this work, we employ ejecta models that consist of two parts; the dynamical ejecta with non-spherical geometry and post-merger ejecta with spherical geometry. In particular, we employ three different types of ejecta profiles. First, we consider the fiducial case in which the post-merger ejecta is slower than the dynamical ejecta. Second, we consider the case in which both ejecta are supposed to be accelerated by an additional energy injection. Third, we consider an ejecta profile model for a BH–NS merger.

Our first ejecta model is composed of a homologously expanding ejecta with its velocity distributing from $v = v_{\rm pm,min}$ to $0.9c$. Here, the post-merger ejecta has the velocity from $v = v_{\rm pm,min}$ to $v_{\rm pm,max}$, and dynamical ejecta from $v = v_{\rm d,min}$ to $0.9c$, $v = r/t$ the velocity of the fluid elements, r the radial coordinate, and t time measured from the onset of a merger. The density profile of each ejecta component is given by

$$\rho(r, t) \propto \begin{cases} r^{-3}t^{-3}, & v_{\rm pm,min} \leqslant r/t \leqslant v_{\rm pm,max} \\ \eta(\theta)r^{-4}t^{-3}, & v_{\rm d,min} \leqslant r/t \leqslant 0.4c, \\ \eta(\theta)r^{-8}t^{-3}, & 0.4c \leqslant r/t \leqslant 0.9c, \end{cases} \quad (3)$$

and a floor value of $10^{-20}(t/{\rm day})^{-3}{\rm g\,cm^{-3}}$ is employed for the density in $v < v_{\rm pm,min}$ and $v_{\rm pm,max} \leqslant v \leqslant v_{\rm d,min}$ (see Figure 2). We employ a broken power-law profile for the radial profile of
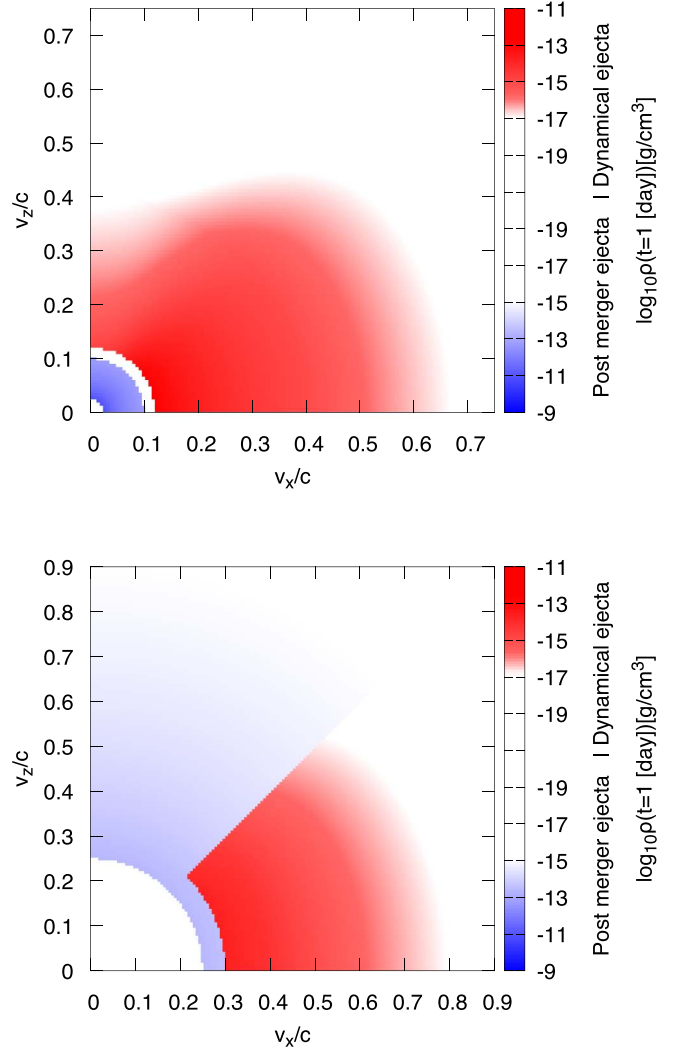

Figure 2. Density profile of the ejecta employed in the radiative transfer simulation for NS–NS merger models. The red and blue regions denote the dynamical and post-merger ejecta, respectively. Homologous expansion of the ejecta and axisymmetry around the rotational axis (z-axis) are assumed in the simulation. The top panel denotes the case of the fiducial model (HMNS_YH) in Table 1, for which we assume that the outer edge of the post-merger ejecta is slower than the inner edge of the dynamical ejecta. The bottom panel denotes the case of SMNS_DYN0.01 in Table 1. In this model, we suppose that the post-merger ejecta is accelerated by the energy injection from the merger remnant.

the dynamical ejecta to model the results obtained by numerical-relativity simulations (Kiuchi et al. 2017; Hotokezaka et al. 2018; see also Figure 3). $\eta(\theta)$ is a function defined by

$$\eta(\theta) = (1 - \Theta(\theta))f_{\rm d,pol} + \Theta(\theta), \quad (4)$$

$$\Theta(\theta) = \frac{1}{1 + \exp[-10(\theta - \pi/4)]}, \quad (5)$$

which is introduced to describe the angular distribution of the dynamical ejecta with θ an angle measured from the polar axis. By employing this function, the density in the polar region ($0 \leqslant \theta \leqslant \pi/4$) is smaller than that in the equatorial region ($\pi/4 \leqslant \theta \leqslant \pi/2$) approximately by a factor of $f_{\rm d,pol}$ (we assume the reflection symmetry with respect to the equatorial plane). We employ $0.025c$ as a fiducial value for $v_{\rm pm,min}$, while
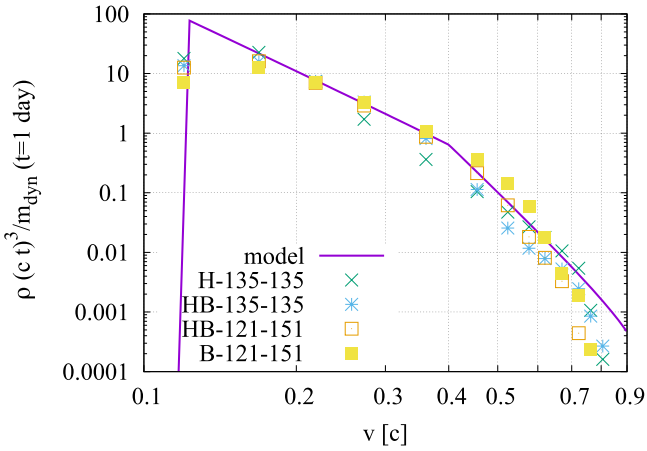
Figure 3. Comparison of the radial density profile of the dynamical ejecta employed in this work (the blue lines) and that obtained by numerical-relativity simulations (data points) (Kiuchi et al. 2017; Hotokezaka et al. 2018).
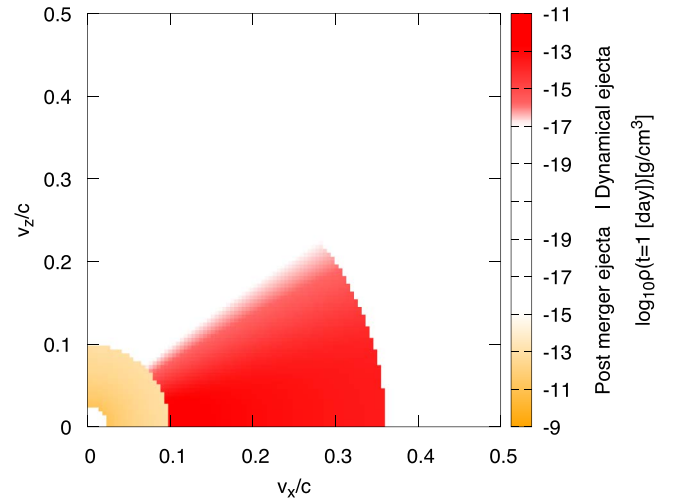

Figure 4. Density profile of the ejecta employed in the radiative transfer simulation for the BH–NS merger ejecta. The density profile of BHNS_A in Table 1 is shown as an example. The red and orange regions denote the dynamical and post-merger ejecta, respectively.

the results depend only weakly on $v_{\mathrm{pm,min}}$ as far as $v_{\mathrm{pm,min}} = 0.025$–$0.05c$. The angular dependence of the density profile and element abundances is not incorporated for the post-merger ejecta for simplicity because it is not significant, as is the case for the dynamical ejecta (Fujibayashi et al. 2018; Fernández et al. 2019).

Following the previous study by Kawaguchi et al. (2018), element abundances are determined employing the results of r-process nucleosynthesis calculations by Wanajo et al. (2014). For the dynamical ejecta in the equatorial region, we employ elements abundances resulting from a flat Y_e distribution in 0.1–0.3. Taking into account the results of Radice et al. (2016), Sekiguchi et al. (2015, 2016), Perego et al. (2017), we gradually change the element abundances to that of a flat Y_e distribution in 0.35–0.44 as the location approaches the polar direction to describe the Y_e angular dependence of the dynamical ejecta. Specifically, the mass fraction of element Z, X_Z, is given by

$$(1 - \Theta(\theta))X_Z(Y_e: 0.35\text{–}0.44) + \Theta(\theta)X_Z(Y_e: 0.1\text{–}0.3), \quad (6)$$

where $X_Z(Y_e: 0.35\text{–}0.44)$ and $X_Z(Y_e: 0.1\text{–}0.3)$ are the mass fractions calculated assuming flat Y_e distributions in 0.35–0.44 and in 0.1–0.3, respectively. For post-merger ejecta, we employ either flat Y_e distributions in 0.3–0.4, 0.2–0.4, or 0.1–0.3 to study the dependence of light curves on the Y_e distribution. We note that the lanthanide mass fractions of flat Y_e distributions in 0.3–0.4, 0.2–0.4, and 0.1–0.3 are $\ll 10^{-3}$, ≈ 0.025, and ≈ 0.14, respectively.

As mentioned earlier, the post-merger ejecta could be accelerated due to an energy injection from the remnant NS after the merger. For this situation, the outer edge of the post-merger ejecta can interact with the inner edge of the dynamical ejecta, and particularly, a fraction of the post-merger ejecta can spread into the polar region of the dynamical ejecta. Hydrodynamical simulations would be needed to obtain a realistic distribution of the ejecta. However, this task is beyond the scope of this work. Instead, for simplicity, we employ the density profile described in Equation (3), allowing the outer edge of the post-merger ejecta, $v_{\mathrm{pm,max}}$, to be larger than the inner edge of the dynamical ejecta, $v_{\mathrm{d,min}}$, but truncating and replacing the post-merger ejecta by the dynamical ejecta for $\theta > \pi/4$ and $v > v_{\mathrm{d,min}}$ to keep the dense part of dynamical

ejecta (see Figure 2). This is our second choice of the ejecta profile.

For a BH–NS merger, the ejecta profile could be different from those for NS–NS mergers, and thus we consider the third profile. For this case, the dynamical ejecta is typically expected to be more confined in the equatorial plane, and the radial density profile is more shallow than that formed in a NS–NS merger. Based on the results of numerical-relativity simulations (Foucart et al. 2017; Kyutoku et al. 2018), we employ the following density profile for the BH–NS ejecta models (see Figure 4):

$$\rho(r, t) \propto \begin{cases} r^{-3}t^{-3}, & 0.025c \leqslant r/t \leqslant 0.1c \\ \tilde{\Theta}(\theta)r^{-2}t^{-3}, & 0.1c \leqslant r/t \leqslant 0.36c \end{cases}, \quad (7)$$

where $\tilde{\Theta}(\theta)$ is given by

$$\tilde{\Theta}(\theta) = \frac{1}{1 + \exp[-20(\theta - 1.2\,[\mathrm{rad}])]}. \quad (8)$$

Here, the outer edge of the dynamical ejecta ($v_{\mathrm{d,max}} = 0.36c$) is determined from the condition that the average velocity of the dynamical ejecta, $\sqrt{2E_{\mathrm{K,d}}/M_{\mathrm{d}}}$, is $0.25c$ with $E_{\mathrm{K,d}}$ the kinetic energy of the dynamical ejecta (Foucart et al. 2017; Kyutoku et al. 2018). For BN-NS mergers, collisional shock heating of the NS or neutrino irradiation from the merger remnant is weak, and hence substantial amount of dynamical ejecta and the post-merger ejecta would have low Y_e values. Taking the prediction obtained by numerical simulations into account (Rosswog et al. 2013; Just et al. 2015; Foucart et al. 2017; Kyutoku et al. 2018), flat Y_e distributions in 0.09–0.11[5] and in 0.1–0.3 are employed for the elements abundances of the dynamical ejecta and the post-merger ejecta, respectively.

---

[5] We note that the Y_e range of 0.09–0.11 is employed due to the limitation in available tables for element abundances and heating rate, while the numerical simulations (Rosswog et al. 2013; Just et al. 2015; Foucart et al. 2017; Kyutoku et al. 2018) predict lower values for Y_e of the dynamical ejecta (typically the lowest value could be ≈ 0.05). Nevertheless, we expect that the resulting lanthanide fraction and heating rate would be different by at most 20%–30% (Lippuner & Roberts 2015).

Table 1
Summary of Ejecta Models Employed for Radiative Transfer Simulations

Model	M_{pm} ($M_\odot$)	M_d ($M_\odot$)	$f_{d,pol}$	$v_{pm}(v_{pm,ave})[c]$	$v_d(v_{d,ave})(c)$	$Y_{e,pm}$	$Y_{e,d}$ (Equatorial/Polar)
HMNS_YH (Fiducial)	0.03	0.01	0.01	0.025–0.1 (0.06)	0.12–0.9 (0.25)	0.3–0.4	0.1–0.3/0.35–0.44
HMNS_YH_DYN0.003	*	0.003	*	*	*	*	*
HMNS_YH_PM0.01	0.01	*	*	*	*	*	*
HMNS_YH_VL	*	*	*	0.025–0.05 (0.04)	0.12–0.9 (0.25)	*	*
HMNS_YH_VH	*	*	*	0.025–0.2 (0.10)	0.2–0.9 (0.33)	*	*
HMNS_YM	*	*	*	*	*	0.2–0.4	*
HMNS_YL	*	*	*	*	*	0.1–0.3	*
GW170817_YM	0.02	0.003	0.0	0.025–0.1 (0.06)	0.12–0.9 (0.25)	0.2–0.4	0.1–0.3/0.35–0.44
GW170817_YH	0.02	0.003	0.0	0.025–0.1 (0.06)	0.12–0.9 (0.25)	0.3–0.4	0.1–0.3/0.35–0.44
BH_PM0.001	0.001	0.001	0.0	0.025–0.1 (0.06)	0.12–0.9 (0.25)	0.1–0.3	0.1–0.3/0.35–0.44
BH_PM0.01	0.01	0.001	0.0	0.025–0.1 (0.06)	0.12–0.9 (0.25)	0.1–0.3	0.1–0.3/0.35–0.44
SMNS_DYN0.01	0.05	0.01	0.01	0.25–0.9 (0.53)	0.3–0.9 (0.41)	0.3–0.4	0.1–0.3/0.35–0.44
SMNS_DYN0.003	0.05	0.003	0.01	0.25–0.9 (0.53)	0.3–0.9 (0.41)	0.3–0.4	0.1–0.3/0.35–0.44
BHNS_A	0.02	0.02	⋯	0.025–0.1 (0.06)	0.1–0.36 (0.25)	0.1–0.3	0.09–0.11
BHNS_B	0.04	0.01	⋯	0.025–0.1 (0.06)	0.1–0.36 (0.25)	0.1–0.3	0.09–0.11
BHNS_DYN	⋯	0.02	⋯	⋯	0.1–0.36 (0.25)	⋯	0.09–0.11
PM_YH	0.03	⋯	⋯	0.025–0.1 (0.06)	⋯	0.3–0.4	⋯
PM_YM	0.03	⋯	⋯	0.025–0.1 (0.06)	⋯	0.2–0.4	⋯
PM_YL	0.03	⋯	⋯	0.025–0.1 (0.06)	⋯	0.1–0.3	⋯
DYN0.01	⋯	0.01	0.01	⋯	0.12–0.9 (0.25)	⋯	0.1–0.3/0.35–0.44
DYN0.003	⋯	0.003	0.01	⋯	0.12–0.9 (0.25)	⋯	0.1–0.3/0.35–0.44

Note. The columns describe the model name, mass of post-merger ejecta M_{pm}, mass of dynamical ejecta M_d, thickness parameter for dynamical ejecta in the polar region $f_{d,pol}$, velocity range of post-merger ejecta $v_{pm,min}$–$v_{pm,max}$, velocity range of dynamical ejecta $v_{d,min}$–$v_{d,max}$, Y_e distribution of post-merger ejecta, and Y_e distribution of dynamical ejecta in equatorial plane/polar axis, respectively. The average velocity calculated by $v_{ave} = \sqrt{2E_K/M}$ is shown in the parenthesis of the columns for ejecta velocity, where E_K and M are the kinetic energy and mass of ejecta, respectively. * denotes that the same value as for the fiducial model (HMNS_YH) is employed.

3.3. Limitation

Before showing the numerical results, we clarify the limitation of our light curve prediction. Employing a new line list, our calculations are applicable for the ejecta of the temperature $\lesssim 20{,}000$ K (Tanaka et al. 2019). However, ejecta temperature can be higher than 20,000 K for $\lesssim 1$ day after the merger particularly for the case where the post-merger ejecta is lanthanide-rich or slow ($\lesssim 0.05c$). Moreover, in the late time of the calculation, assuming the LTE, which we impose to determine the temperature, emissivity, and so on could be no longer valid. For the typical cases that we study in this work, the post-merger ejecta becomes completely optically thin for $\gtrsim 10$ days for lanthanide-free cases. Thus, we will mainly focus on the results for 1 days $\leqslant t \leqslant 10$ days.

3.4. Models

In Table 1, we summarize the models and their parameters studied in this paper (see also Figure 1). HMNS_YH corresponds to a model for which high-Y_e post-merger ejecta is supposed to be formed due to neutrino irradiation from a long-surviving remnant NS. We set HMNS_YH as the fiducial setup. HMNS_YH_DYN0.003 and HMNS_YH_PM0.01 are the models with smaller dynamical ejecta mass and smaller post-merger ejecta mass than the fiducial model, respectively. These models are employed to study the mass dependence of the light curves. HMNS_YH_VL and HMNS_YH_VH are the models with lower velocity for post-merger ejecta and higher velocity for both ejecta components than the fiducial model, respectively.

HMNS_YM and HMNS_YL are the models with same mass and velocity parameters as in the fiducial model but with low-Y_e distributions for post-merger ejecta ($Y_e = 0.2$–0.4 and 0.1–0.3, respectively) employed to study the light curves in the presence of lanthanides in the post-merger ejecta. They model the cases in which the remnant collapses to a BH in a short timescale (a few ms) after the merger. GW170817_YM and GW170817_YH are the models of which ejecta parameters are chosen to reproduce the peak brightness of the optical and infrared counterpart to GW170817.

BH_PM0.001 and BH_PM0.01 are the models with lanthanide-rich post-merger ejecta of small masses. They model the cases in which the NSs collapse to a BH promptly after the merger and the dynamical ejecta mass and the torus mass of the remnant are suppressed as a consequence (Kiuchi et al. 2009; Hotokezaka et al. 2013). In reference to the results of the prompt-collapse case in previous studies (e.g., Kiuchi et al. 2009; Hotokezaka et al. 2013; Kiuchi et al. 2019), $0.001\,M_\odot$ and $0.01\,M_\odot$ are employed as the post-merger ejecta mass for BH_PM0.001 and BH_PM0.01, respectively, while the dynamical ejecta mass is set to be $0.001\,M_\odot$ for both BH_PM0.001 and BH_PM0.01. According to previous studies, post-merger ejecta is expected to be lanthanide-rich due to the absence of neutrino irradiation from the remnant NS (Metzger & Fernández 2014; Wu et al. 2016; Lippuner et al. 2017; Siegel & Metzger 2017; Fernández et al. 2019). Thus, we employ a flat distribution of $Y_e = 0.1$–0.3 for the post-merger ejecta.

SMNS_DYN0.01 and SMNS_DYN0.003 are the models composed of high-velocity post-merger ejecta. For these models, we suppose that the ejecta is accelerated by the energy injection from a long-surviving SMNS. In this study, we consider that the average velocity of the post-merger ejecta and dynamical ejecta are $\approx 0.5c$ and $\approx 0.4c$, respectively (see Table 1). These values correspond to the cases for which $\approx 1 \times 10^{52}$ erg of the rotational kinetic energy of remnant NS is converted to the ejecta kinetic energy. We set the post-merger ejecta mass to $0.05\,M_\odot$ because the remnant torus mass would be large for a NS–NS merger, which results in the long-surviving SMNS. $0.01\,M_\odot$ and $0.003\,M_\odot$ are employed for the dynamical ejecta mass for SMNS_DYN0.01 and SMNS_DYN0.003, respectively. We note that the latter would be consistent with the prediction of numerical simulations because relatively small dynamical ejecta mass is typically predicted for a NS–NS binary with small total mass (Foucart et al. 2016).

BHNS_A, BHNS_B and BHNS_DYN are the models for the BH–NS ejecta of density profile described in Equation (7). As mentioned earlier, the mass of the dynamical ejecta and the remnant torus strongly depend on the binary parameters. In this paper, we specifically study the models with $(M_{pm}, M_d) = (0.02\,M_\odot, 0.02\,M_\odot)$ (BHNS_A) and $(0.04\,M_\odot, 0.01\,M_\odot)$ (BHNS_B) in reference to the results of ALF2-Q7a75 and H4-Q3a0 in Kyutoku et al. (2015), respectively, for which massive ejecta and remnant torus are formed as a result of NS tidal disruption. Here, we assume that $\approx 40\%$ of the remnant torus mass is ejected as the post-merger ejecta. In addition to these models, we only show the results of the BH–NS model with a dynamical ejecta of mass $0.02\,M_\odot$, while employing the ejecta density profile described in Equation (7) (BHNS_DYN) to understand the basic properties of the light curves caused by the BH–NS dynamical ejecta.

PM_YH, PM_YM, PM_YL, DYN0.01, and DYN0.003 are models with only post-merger ejecta or dynamical ejecta for NS–NS mergers. These models are calculated to understand the basic properties of the light curves determined by each ejecta component. The results for these models are summarized in the appendix.

4. Effects of Multiple Ejecta Components

In this section, we study how large the effect of radiative transfer of photons in the multiple ejecta components could be and we show the light curves' dependence on the ejecta parameter.

4.1. Fiducial Model

The effect of the radiative transfer of photons in the multiple ejecta components has a large impact on the resulting light curves. There are three effects that take place by consistently solving the photon radiation transfer in the multiple ejecta components. The first effect is to enhance the flux in the polar direction (see the left-hand panel of Figure 5). In the presence of optically thick dynamical ejecta concentrated near the equatorial region, photons emitted from the post-merger ejecta at an early time ($\lesssim 3$–5 days) preferentially diffuse in the polar direction, and this effectively enhances the energy flux observed from the polar region. The second effect is to block the emission from post-merger ejecta by the dynamical ejecta (Kasen et al. 2015) (see the middle panel of Figure 5). Because the post-merger ejecta is surrounded by an optically

thick dynamical ejecta, photons emitted from the post-merger ejecta cannot directly diffuse to the equatorial direction. This results in the strong suppression of the energy flux in the optical wavelengths observed from the equatorial direction. The third effect is to heat the dynamical ejecta by the post-merger ejecta (see the right-hand panel of Figure 5). A fraction of the photons emitted from the post-merger ejecta is absorbed and becomes an additional heating source for the dynamical ejecta. Absorbed photons are re-emitted from the dynamical ejecta and enhance the flux, particularly in the infrared wavelengths.

As an illustration, we show the results of the radiative transfer simulation for the HMNS_YH model in Figure 6. The *grizJHK*-band light curves observed from the polar direction ($0° \leqslant \theta \leqslant 20°$, the top panels) and the equatorial direction ($86° \leqslant \theta \leqslant 90°$, the bottom panels) are shown in Figure 6. Here, the solid and dashed curves denote the light curves obtained by the simulation in which the radiative transfer effect of photons in the multiple ejecta components is taken into account (which we refer to as the full calculation in the following) and the calculation in which each ejecta component is treated separately and superimposed afterward, respectively. For the light curves observed from the polar direction, both the optical and the infrared emissions are brighter for the full calculation than for the superimposed model. This clearly shows that photons preferentially diffuse out toward the polar direction. The photon fluxes are enhanced typically by ≈ 0.5–1 mag, particularly for the early phase ($t \lesssim 7$ days). This indicates that ejecta mass could be overestimated by $\approx 50\%$–100% if the radiative transfer effect of photons in the multiple ejecta components is not taken into account for the mass estimation from observed light curves.

The enhancement of the *JHK*-band flux is most significant after ≈ 2 days, while it is less significant in the earlier time. This implies that the *JHK*-band light curves after ≈ 2 days of the full calculation are dominated by the emission from the post-merger ejecta reprocessed in the dynamical ejecta. Meanwhile, the less significant enhancement of the *JHK*-band flux for $\lesssim 2$ days indicates that the emission powered by the radioactive heating in the dynamical ejecta also has a significant contribution to the *JHK*-band light curves in such an early phase. This reflects the fact that, for the fiducial model, the photon reprocessing is not efficient for the early phase because of the long diffusion timescale of the dynamical ejecta of mass $\gtrsim 10^{-3}\,M_\odot$ (see Equation (2)).

For the light curves observed from the equatorial direction, the *griz*-band emission is strongly suppressed in the full calculation, while that in the separately calculated model is as bright as that observed from the polar direction. This is due to the blocking effect of optical photons from the post-merger ejecta by the dynamical ejecta (Kasen et al. 2015; Bulla 2019). Indeed, the suppression of the optical bands becomes significant for $\theta \geqslant 45°$, which reflects the employed opening angle of the dynamical ejecta (see Figure 7). Meanwhile, the *HK*-band emission is brighter for the full calculation than the other, particularly after ≈ 3 days. This is due to the heating of the dynamical ejecta by the post-merger ejecta. The angular dependence of the infrared light curves is much weaker than that of the optical light curves. This implies that the infrared emission is dominated by photons emitted from or reprocessed in the dynamical ejecta.
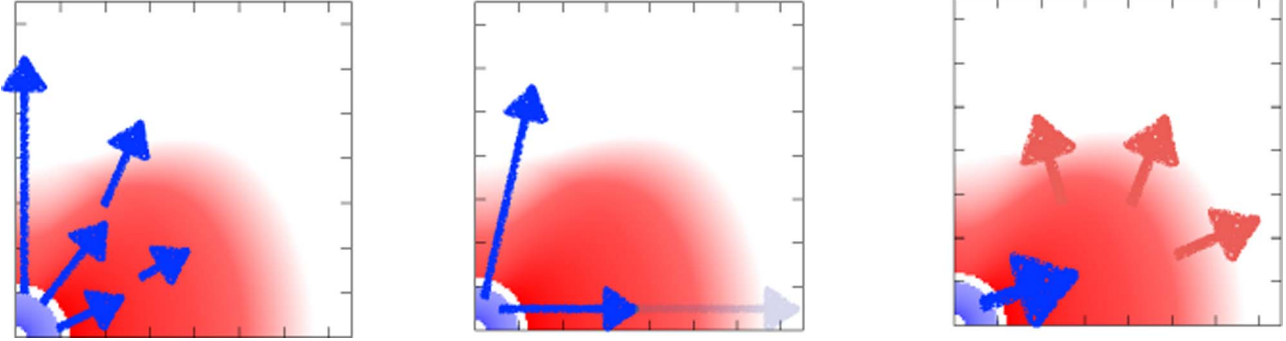
(i) Diffusion preferentially in the polar direction　　(ii) Blocking effect　　(iii) Heating up of the dynamical ejecta

Figure 5. Schematic picture for the effects that are incorporated by taking the radiative transfer of photons in the multiple ejecta components into account (see the main text for the detail). Preferential diffusion of photons in the polar direction (left-hand panel). Blocking effect of the emission from post-merger ejecta by the dynamical ejecta (middle panel). Heating of the dynamical ejecta by the post-merger ejecta (right-hand panel).

4.2. Mass Dependence

Figure 8 shows the *grizJHK*-band light curves for a small dynamical ejecta mass model (HMNS_YH_DYN0.003) and a small post-merger ejecta model (HMNS_YH_PM0.01), as well as the fiducial model (HMNS_YH) as a reference. We found that the *griz*-band light curves show approximately the same brightness as in the fiducial case for $t \lesssim 2$ days due to the enhancement of the optical brightness by photon diffusion preferentially in the polar direction, as long as $M_{\rm d} \geqslant 0.001\,M_{\odot}$. Meanwhile, this effect fades earlier than the fiducial case for the small dynamical ejecta mass case because of its shorter diffusion timescale. Indeed, for the light curves observed from the polar direction, the *griz*-band brightness for the small dynamical ejecta mass (HMNS_YH_DYN0.003) and fiducial model agree with each other within ≈ 0.2 mag for 1 day $\leqslant t \leqslant$ 2.5 days, while the brightness becomes fainter after ≈ 2.5 days. Note that, exceptionally, the *g*-band emission is slightly brighter than the fiducial model, particularly for $t \gtrsim 2$ days, due to the decrease in the density of dynamical ejecta in the polar region.

The brightness of the *JHK*-band light curves does not necessarily reflect the mass of the dynamical ejecta but could depend strongly on the mass of post-merger ejecta. The *JHK*-band emission of the small dynamical ejecta mass model (HMNS_YH_DYN0.003) is only by ≈ 0.5 mag fainter than that of the fiducial model, though the dynamical ejecta mass is different by a factor of ≈ 3. This happens because photons emitted from the post-merger ejecta are reprocessed more efficiently from the earlier phase for the smaller dynamical ejecta mass model due to shorter diffusion timescale. Nevertheless, the *JHK*-band brightness still could provide the upper limit to the dynamical ejecta mass, and the results above indicate that using data observed for the early phase $\lesssim 2$ days might be the better choice for constraining the dynamical ejecta mass because the contribution of reprocessed photons from the post-merger ejecta is relatively less significant than that for the later phase.

The brightness of the light curves for a small post-merger ejecta mass case is typically faint due to the decrease in the heating source (HMNS_YH_PM0.01). Indeed, the *griz*-band emission for HMNS_YH_PM0.01 is fainter than that of the fiducial model and the small dynamical ejecta mass model

(HMNS_YH_DYN0.003). The *JHK*-band emission for the later phase ($\gtrsim 2$ days) is also fainter for HMNS_YH_PM0.01 than the other models because it is dominated by the emission from the post-merger ejecta reprocessed in the dynamical ejecta. Exceptionally, the *JHK*-band emission for HMNS_YH_PM0.01 is slightly brighter than HMNS_YH_DYN0.003 in the early time $\lesssim 2$ days. This happens because HMNS_YH_PM0.01 has larger dynamical ejecta mass than HMNS_YH_DYN0.003, while the radioactive heating in the dynamical ejecta also contributes to the *JHK*-band light curves for $\lesssim 2$ days.

For the light curves observed from the equatorial direction, the *griz*-band energy flux is strongly suppressed due to the blocking effect of the dynamical ejecta. All of the cases exhibit approximately the same light curves and are not distinguishable by the optical light curves. In addition, the *JHK*-band emission observed in the equatorial direction is fainter by ≈ 1 mag than in the polar direction but the light curves show the same feature as those observed from the polar direction, and the dependence on the ejecta mass is clearly reflected.

4.3. Velocity Dependence

Figure 9 compares the *grizJHK*-band light curves among the models with the same ejecta mass as in the fiducial model (HMNS_YH) but with different velocity parameters. The model with slow-velocity post-merger ejecta (HMNS_YH_VL) shows slightly longer-lasting light curves than the fiducial model due to the longer diffusion timescale (e.g., Equation (2)). Meanwhile, the light curves for the model of which both post-merger and dynamical ejecta have higher velocity than the fiducial model (HMNS_YH_VH) decline much earlier than the fiducial model due to the short diffusion timescale of ejecta. The rapid decline is particularly significant for the *griz*-band light curves, although the peak magnitudes in all the grizJHK bands are approximately the same as in the fiducial model for HMNS_YH_VL and the difference from the fiducial model is smaller than ≈ 0.2 mag. The peak brightness of HMNS_YH_VH also agrees with that of the fiducial model within ≈ 0.3 mag in all the grizJHK bands. These results indicate that the difference in the velocity profile is reflected most significantly in the decline rates of the light curves, particularly in the optical (and perhaps, also, ultraviolet) bands. We note that the rapid decline of the optical light curves for HMNS_YH_VH may reflect the fact
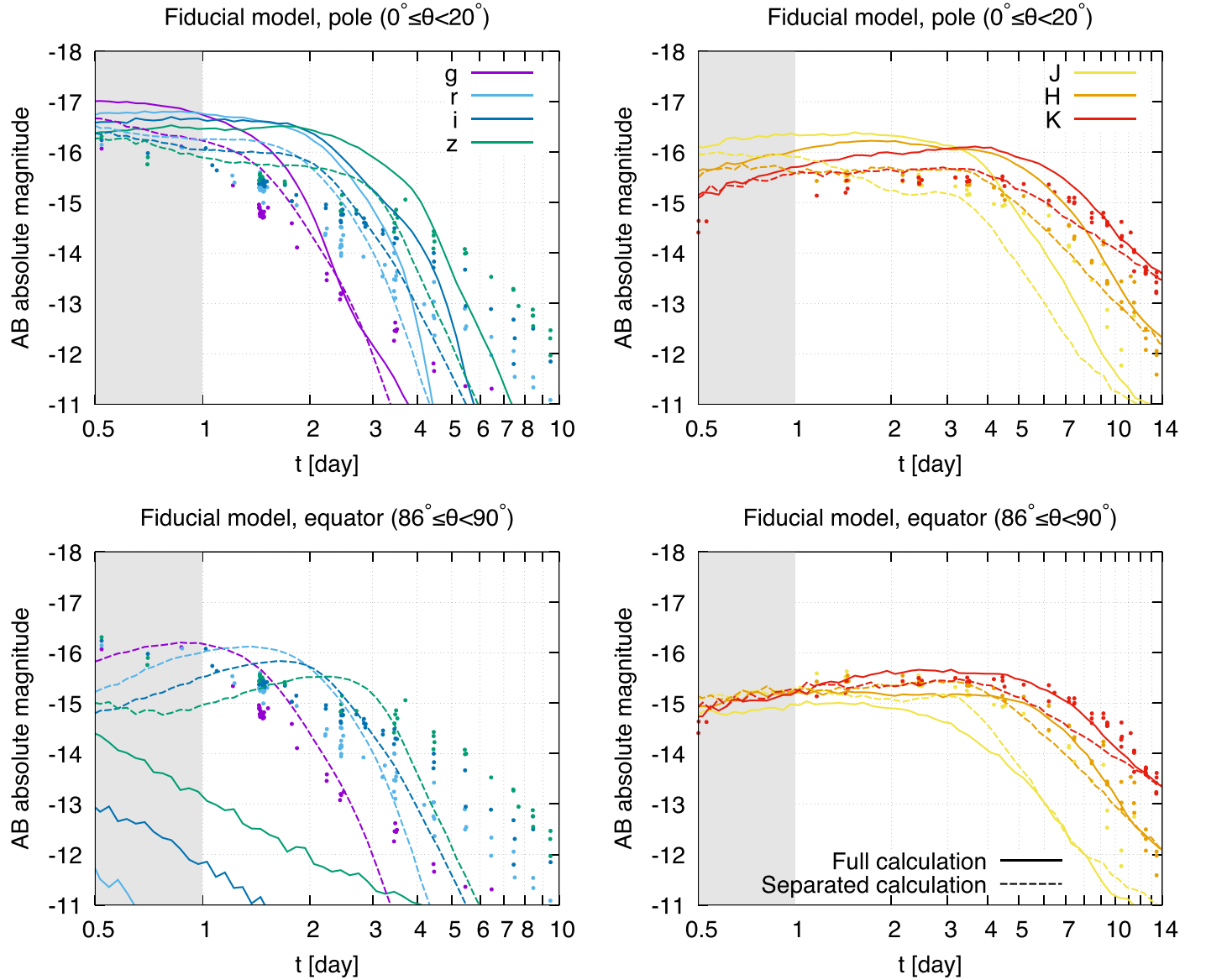
Figure 6. The *grizJHK*-band light curves for the fiducial model (`HMNS_YH`). The solid and dashed curves denote the light curves obtained by the calculation in which both post-merger and dynamical ejecta are solved together, in which each ejecta component are calculated separately and superimposed, respectively. Top and bottom panels denote the light curves observed from the polar ($0° \leqslant \theta \leqslant 20°$) and equatorial direction ($86° \leqslant \theta \leqslant 90°$), respectively. The left-hand and right-hand panels denote the *griz* and *JHK*-band light curves, respectively. The optical and infrared data points in GW170817 taken from Villar et al. (2017) are shown as a reference assuming 40 Mpc for the distance to the event. The early parts of the light curves that are shaded in gray color ($t \leqslant 1$ days) are the phase in which our calculations are not reliable because the ejecta temperatures are too high.

that the opacity depends strongly on the temperature near $T \approx 3000$ K and the temperature of the post-merger ejecta for `HMNS_YH_VH` decreases more steeply than for other models.

For the light curves observed from the equatorial direction, the difference from the fiducial model is only remarkable for `HMNS_YH_VH`. This reflects the fact that the light curves observed from the equatorial direction are dominated by the emission from the dynamical ejecta because the density profiles of the dynamical ejecta for `HMNS_YH_VL` and the fiducial model are the same.

4.4. Y_e Dependence

Figure 10 shows the *grizJHK* light curves of the models with lanthanide-free (`HMNS_YH`; solid curves, $X_{pm,lan} \ll 10^{-3}$), mildly lanthanide-rich (`HMNS_YM`; dashed curves, $X_{pm,lan} \approx 0.025$), and highly lanthanide-rich (`HMNS_YL`; dotted curves, $X_{pm,lan} \approx 0.14$)

post-merger ejecta (here, $X_{pm,lan}$ denotes the lanthanide mass fraction of the post-merger ejecta). For the light curves observed from the polar direction, the *griz*-band emission grows faint and shows a shallow decline as the lanthanide fraction of the post-merger ejecta increases. These can be understood by the fact that diffusion timescale of the post-merge ejecta is longer for the lower-Y_e models due to the large opacities. We note that the Y_e dependence of the heating rate is also an important reason for the difference in the light curves particularly for the late phase ($t \gtrsim 5$ days) (see Figure 11).

We find that the optical light curves observed from the polar direction are dominated by the emission from the post-merger ejecta, as long as its mass is larger than that of dynamical ejecta. This indicates that the observed brightness in the *griz*-band would be used to constrain the post-merger ejecta mass. We note that, as is found in the fiducial model, the optical
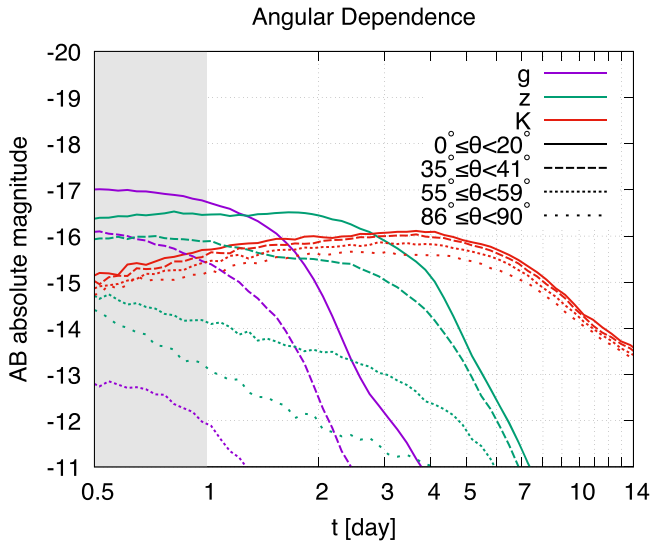
Figure 7. Angular dependence of the *gzK*-band light curves for the fiducial model (`HMNS_YH`). The solid, dashed, densely dotted, and sparsely dotted curves denote the light curves observed from $0° \leqslant \theta < 20°$, $35° \leqslant \theta \leqslant 41°$, $55° \leqslant \theta < 59°$, and $86° \leqslant \theta < 90°$, respectively.

emission for the lanthanide-rich post-merger ejecta (`HMNS_YM` and `HMNS_YL`) is also brighter than that for the models purely composed of the post-merger ejecta (`PM_YM` and `PM_YL`), due to the preferentially diffusion of the photon in the polar direction (see Figure 19). Thus, the enhancement of the brightness due to diffusion in the preferential direction should be taken into account for the ejecta mass estimation and also for the case with lanthanide-rich post-merger ejecta.

For all of the models, the brightness in the *JHK*-bands observed from the polar direction agrees with each other within ≈0.1 mag for ≲3 days. Meanwhile, the low-Y_e models show brighter *JHK*-band emission than the fiducial model after ≈5 days, and much brighter emission is seen in the lanthanide-rich model (`HMNS_YL`). This indicates that the lanthanide fraction of the post-merger ejecta would be reflected in the *JHK*-band light curves for the late phase. However, we note that this enhancement in the *JHK*-band brightness for the late phase for the lanthanide-rich post-merger ejecta models is not only due to the bright infrared emission directly emitted from the post-merger ejecta but is also due to the strong heating to the dynamical ejecta by the post-merger ejecta because the heating rate is larger for the lower-Y_e model, particularly for the late phase (see Figure 11). Indeed, we found that the *JHK*-band emission at ≳5 days for the fiducial model is as bright as that for the mildly lanthanide-rich case (`HMNS_YM`) shown in Figure 10 if the same heating rate for the post-merger ejecta is employed. This indicates that employing reliable heating rate model, particularly for the late phase, would be crucial for measuring the lanthanide fractions of ejecta from the infrared light curves.

As is the case for the ejecta mass dependence, Y_e dependence of the light curves observed from the equatorial direction is only remarkable in the infrared light curves. The *griz*-band emission is strongly suppressed and the emission among different Y_e models is not distinguishable. Meanwhile, the difference in the *JHK*-band light curves among different Y_e models is clearly seen as in those observed from the polar direction for $t \gtrsim 6$ days.

5. Model Parameters for Interpreting GW170817

In this section, we discuss which model parameters would be suitable to interpret the observed optical and infrared light curves in GW170817. We focus only on the light curves observed from the direction close to the polar axis because the GW data analysis of GW170817 infers that the event is observed from $\theta \lesssim 28°$ (Abbott et al. 2017b).

For our ejecta profile setup, we find that the post-merger ejecta is required to explain the brightness in the *griz*-band. Indeed, we confirm that the *griz*-band emission with the dynamical ejecta alone is too faint to interpret the observational results as long as we assume $M_d \leqslant 0.01\,M_\odot$ (see Figure 20 in the appendix). The results obtained with only post-merger ejecta suggest that the mass of ≈0.03 $M_\odot$ would be suitable to interpret the brightness in *griz*-band (see Figure 19 in the appendix). Meanwhile, a smaller mass is preferred for the multi-components model due to the effect of the diffusion of photons preferentially in the polar direction. Indeed, the fiducial model (`HMNS_YH`), in which post-merger ejecta is lanthanide-free with mass 0.03 $M_\odot$, overproduces the *griz*-band brightness for the early phase (≲2 days). This suggests that the post-merger ejecta mass less than 0.03 $M_\odot$ is preferred for our setup if it is lanthanide-free ($X_{pm,lan} \ll 10^{-3}$).

To interpret the observed brightness in the *griz*-band, a larger mass would be allowed for lanthanide-rich post-merger ejecta than lanthanide-free case because *griz*-band emission is fainter for these models. However, lanthanide-rich post-merger ejecta that is too massive would also be unsuitable because it overproduces the *JHK*-band brightness for the late phase ($t \gtrsim 7$ days). Indeed, even in the absence of the dynamical ejecta, the model with highly lanthanide-rich post-merger ejecta (`PM_YL`, $X_{pm,lan} \approx 0.14$) overproduces the *JHK*-band brightness for $t \gtrsim 7$days, while the *griz*-band brightness is underproduced. This indicates that the lanthanide fraction of the post-merger ejecta is likely to ≪0.1 for interpreting the observed light curves in GW170817.

A tighter upper limit to the dynamical ejecta mass is better obtained for multi-component models than a model with only the dynamical ejecta. The result of a model with only the dynamical ejecta (`DYN0.01`) shows that $M_d \lesssim 0.01\,M_\odot$ is preferred not to overproduce the observed *JHK*-band light curves for $t \lesssim 3$ days (see Figure 20 in the appendix). Figure 8 shows that the model with $M_d \lesssim 0.003\,M_\odot$ is consistent with the observed *JHK*-band light curves, particularly for the early phase ($t \lesssim 4$ days) if the post-merger ejecta mass is ≈0.03 $M_\odot$. This shows that the enhancement of the infrared brightness due to the heating effect to the dynamical ejecta by the post-merger ejecta is important in the presence of multi-components.

Motivated by this discussion, we select two models, `GW170817_YM` and `GW170817_YH`, which reproduce the peak brightness observed in GW170817. Figure 12 shows the light curves with mildly lanthanide-rich post-merger ejecta (`GW170817_YM`, $X_{pm,lan} \approx 0.025$) and with lanthanide-free post-merger ejecta (`GW170817_YH`, $X_{pm,lan} \ll 10^{-3}$) observed from $0° \leqslant \theta < 20°$ and $20° \leqslant \theta < 28°$, respectively. For both models, the mass of dynamical and post-merger ejecta are $0.003\,M_\odot$ and $0.02\,M_\odot$, respectively. Both models shown in Figure 12 reproduce the peak brightness observed in GW170817. In particular, `GW170817_YM` reproduces the observed brightness of the optical light curves for the early phase ($t \lesssim 2$ days), even for the case that the post-merger ejecta is mildly lanthanide-rich. This indicates that the post-merger
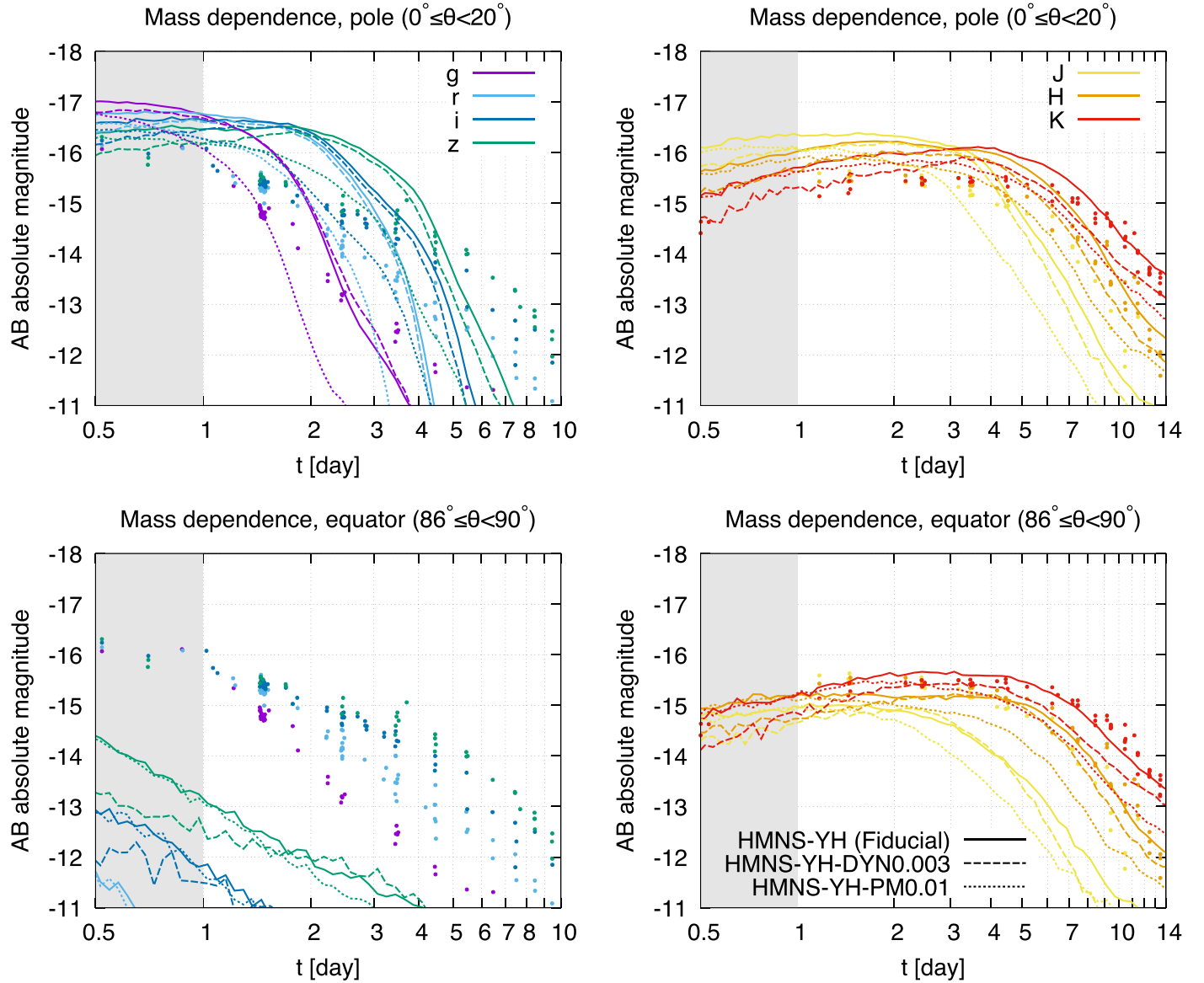
Figure 8. The *grizJHK*-band light curves for the fiducial model and the models with different ejecta mass. The solid, dashed and dotted curves denote the fiducial model (HMNS_YH), the model with small dynamical ejecta mass (HMNS_YH_DYN0.003), and the model with small post-merger ejecta mass (HMNS_YH_PM0.01), respectively. For reference, we also plot the data points of GW170817 (Villar et al. 2017).

ejecta is not necessarily required to be completely lanthanide-free to interpret the observed peak brightness in the optical bands (Kasen et al. 2017; Perego et al. 2017). Moreover, *HK*-band light curves that are consistent with the observation are obtained for the model with mildly lanthanide-rich post-merger ejecta, while the model with lanthanide-free post-merger ejecta underproduces the observed light curves for the late phase ($t \approx 5$ days). Thus, the model with mildly lanthanide-rich post-merger ejecta is preferred to interpret the observation for our setup.

The lanthanide-rich post-merger ejecta could also be well-suited for interpreting the featureless spectrum found in the early part of the observation. Figure 13 shows the spectra of GW170817_YM and GW170817_YH at $t \approx 1.5$ days and $t \approx 3.5$ days together with the observed data. The spectrum with mildly lanthanide-rich post-merger ejecta (GW170817_YM) exhibits much fewer features than that with lanthanide-free one (GW170817_YH). We find that this is also the case for the later phase ($t \gtrsim 3.5$ days). This is a

consequence of the huge number of spectral line mixing, and thus, this indicates that high-velocity ejecta is not necessarily required to reproduce the observed featureless spectrum unless the line emitting region is lanthanide-free. We also note that this shows the importance of employing the complete atomic line list for the light curve prediction.

We note, however, that there is a drawback in these models. Neither models reproduce the *grizJ*-band light curves for $t \gtrsim 2$–4 days due to too steep decline in the model light curves. Both models in Figure 12 exhibit a decline feature that is too fast and is exponential-like in the *griz*-band light curves compared to the observation (see also the spectrum for $\lesssim 7000$ Å at 3.5 day in Figure 13). In contrast, the observed *griz*-band light curves of GW170817 exhibits approximately power-law like decline for the late phase. It is natural to have an exponential-like decline feature by employing the power-like heating rate because the spectrum declines exponentially in the high-frequency part if the spectrum is approximately the blackbody. Indeed, a similar drawback is also
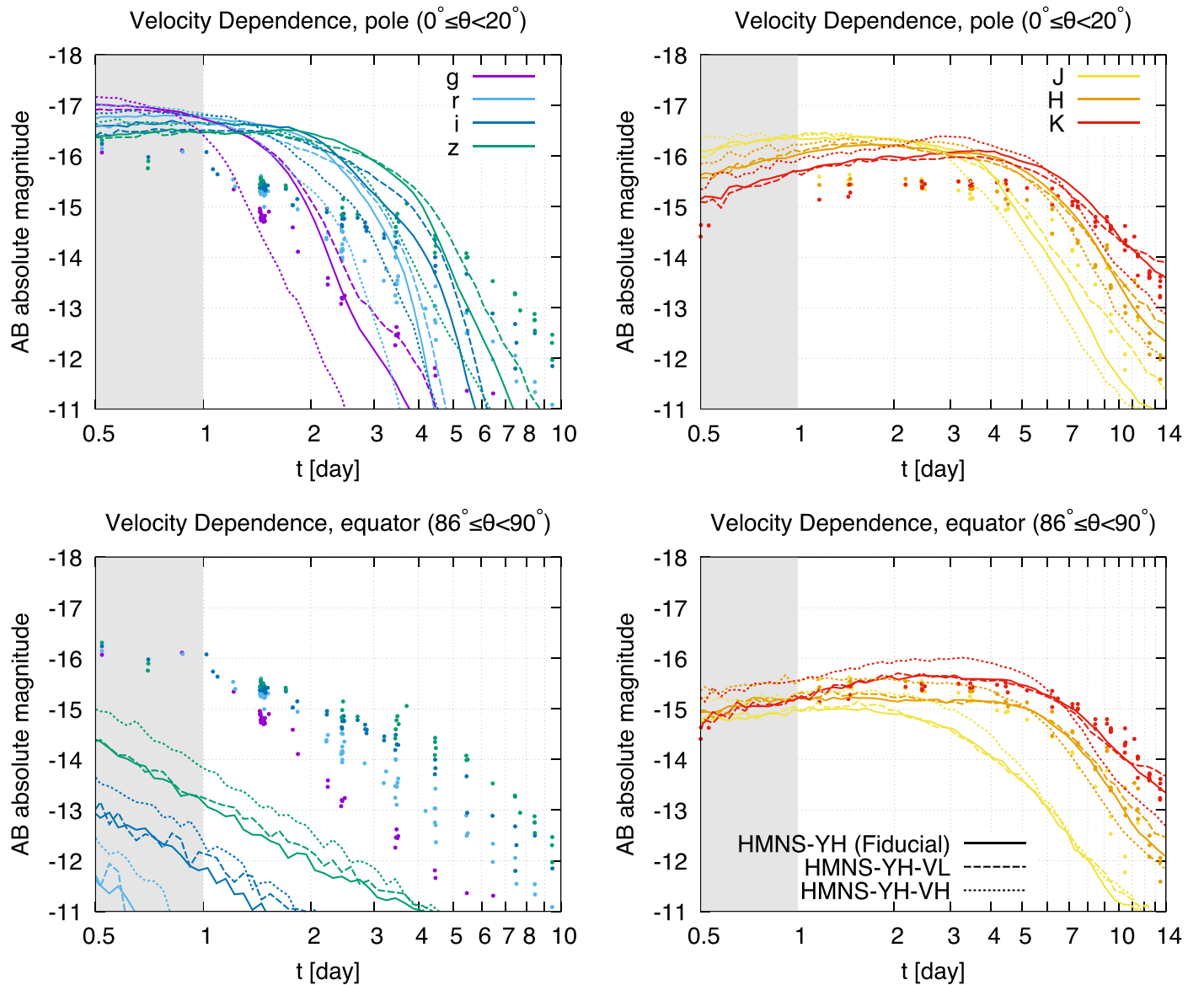
Figure 9. The *grizJHK*-band light curves for the fiducial model and the models with the different ejecta velocity. The solid, dashed, and dotted curves denote the fiducial model (HMNS_YH), the model with slow-velocity post-merger ejecta (HMNS_YH_VL), and the model with high-velocity post-merger and dynamical ejecta (HMNS_YH_VH), respectively. For reference, we also plot the data points of GW170817 (Villar et al. 2017).

found in the model proposed in Waxman et al. (2018), although the ejecta configuration, treatment of radiative transfer, and the energy deposition rate are different from our model (see Figure 10 in the reference). The observed power-law like decline of the optical light curves for the late phase may indicate that additional ejecta components of which diffusion timescales are different from the post-merger ejecta models may be needed to explain the *griz*-band light curves below $\gtrsim -14$ mag or $m_{app} \gtrsim 19$ mag, where m_{app} denotes the apparent magnitude. For example, a power-law like feature for the late phase is described by the superposition of light curves from three ejecta components with different diffusion timescales for the model proposed in Villar et al. (2017) (see Figure 4 in the reference).

Alternatively, this issue may be due to our assumption for the heating rate. The model of the radioactive heating rate that we employ for the post-merger ejecta is derived based on a nucleosynthesis calculation for the dynamical ejecta (Wanajo et al. 2014), but in reality it may differ from that for the

post-merger ejecta due to the difference in ejecta composition, entropy and velocity (Lippuner & Roberts 2015; Wanajo 2018; Wanajo et al. 2018). In addition, the LTE assumption, which we assume to determine the ejecta temperature, would not be valid in the late phase because the density becomes low. Thus, we note that the behavior of the light curves for the late phase, as well as the ejecta mass suitable for interpreting the observational results could change from the current results if a more realistic heating rate model is employed or the non-LTE effect is taken into account.

6. Kilonova Light Curves in Various NS Mergers

In the previous section, we presented models that could capture the features for the light curve of GW170817. These models are considered to be typical models for the case that a HMNS is formed after the merger of binary neutron stars. In
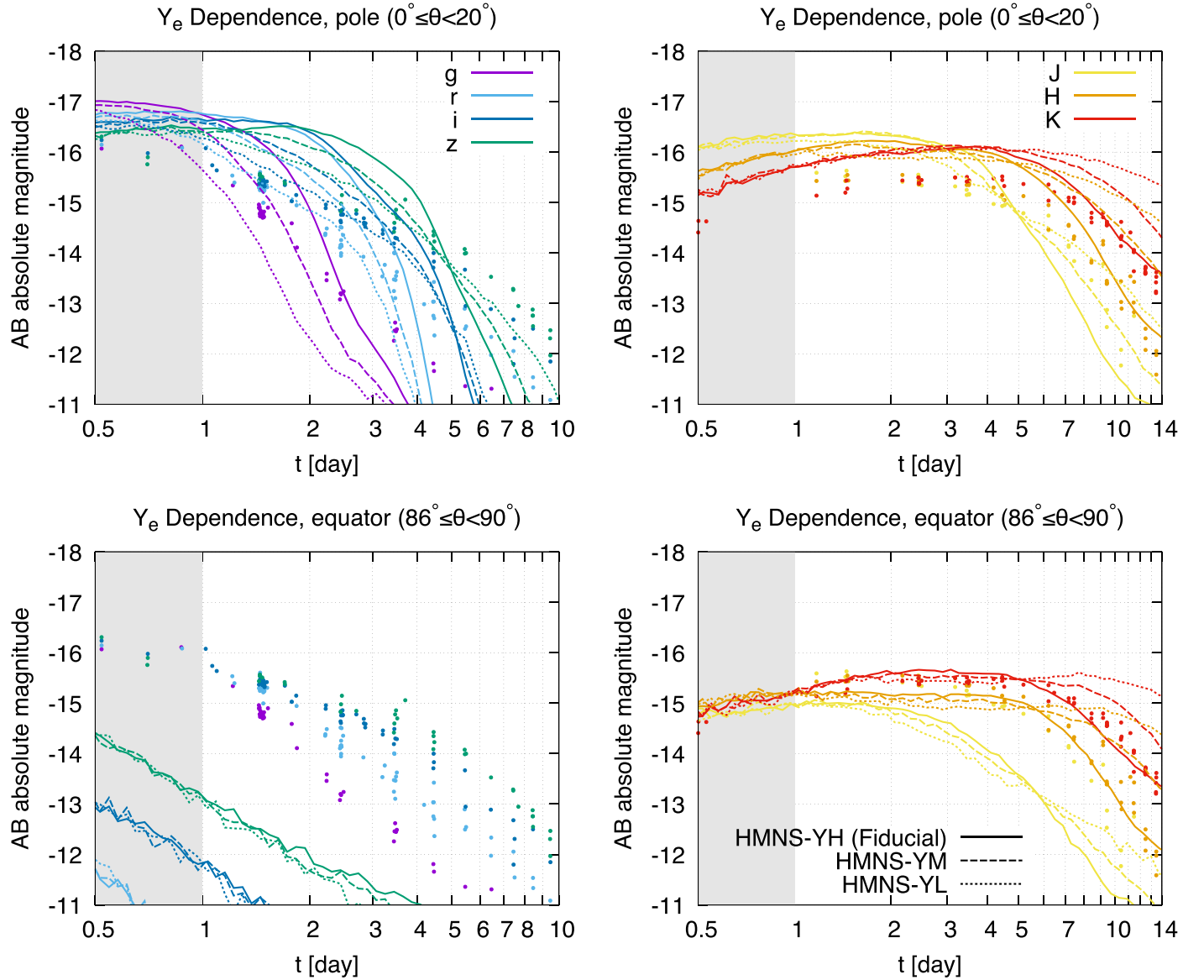
Figure 10. The *grizJHK*-band light curves for lanthanide-free (`HMNS_YH`; solid curves, $X_{pm,lan} \ll 10^{-3}$), mildly lanthanide-rich (`HMNS_YM`; dashed curves, $X_{pm,lan} \approx 0.025$), and highly lanthanide-rich (`HMNS_YL`; dotted curves, $X_{pm,lan} \approx 0.14$) post-merger ejecta. Here, $X_{pm,lan}$ denotes the lanthanide mass fraction of the post-merger ejecta. For reference, we also plot the data points of GW170817 (Villar et al. 2017).

this section, we show the predicted light curves for a variety of NS mergers.

6.1. Prompt Collapse Cases

Figure 14 shows the *grizJHK*-band light curves for prompt-collapse ejecta models in which a BH is supposed to be immediately formed after the onset of NS–NS merger. The dynamical ejecta mass is set to be $0.001\,M_\odot$ for both `BH_PM0.001` and `BH_PM0.01`, and the post-merger ejecta mass is set to be $0.001\,M_\odot$ and $0.01\,M_\odot$ for `BH_PM0.001` and `BH_PM0.01`, respectively. These values are motivated by the numerical results that the ejecta mass is suppressed for the prompt-collapse case (Hotokezaka et al. 2013). Kilonovae for these models are fainter than those in the HMNS formation case shown in Section 4 because of the small ejecta mass. Indeed, the peak brightness of the *griz*-band light curves is always fainter than -16 mag. However, for the model with a

post-merger ejecta mass of $0.01\,M_\odot$, the *riz*-band emission remains brighter than -13 mag (which corresponds to $m_{app} = 20$ mag for the distance of 40 Mpc) until 2–3.5 days after the merger, due to its relatively larger mass and longer diffusion timescale. This indicates that the *riz*-band emission for $t \lesssim 3$ days would be observed by 1 m class telescopes, such as ZTF (Bellm & Kulkarni 2017),[6] even for the prompt-collapse cases if the event occurs as close as in GW170817 and is observed close to face-on. Meanwhile, for the model of which post-merger ejecta mass is $0.001\,M_\odot$, the *griz*-band emission becomes fainter than -11 mag within 2 days. The optical emission observed from the equatorial direction is completely blocked by the dynamical ejecta, even for the case where the dynamical ejecta is not massive $0.001\,M_\odot$. Thus, if the post-merger ejecta is much smaller than $0.01\,M_\odot$ or the event is observed from the equatorial direction, then the

---

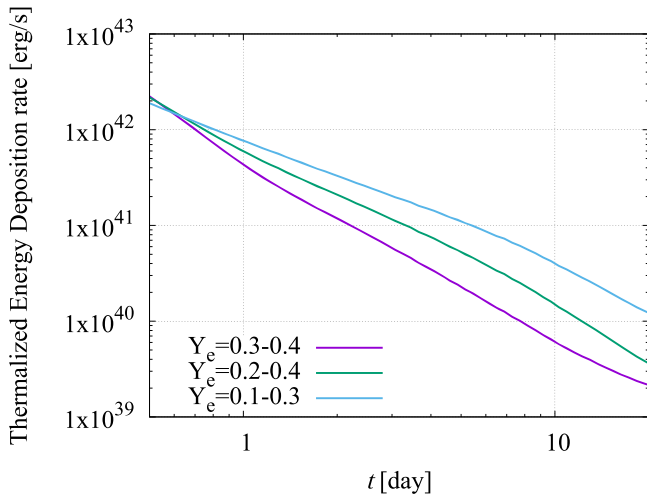[6] We assume the limiting magnitude to be $m_{app} = 20$ mag.

Figure 11. Comparison of the energy deposition rates among the post-merger ejecta models with different Y_e distributions (PM_YH, PM_YM, and PM_YL). The energy deposition rates are shown after thermalization efficiency is taken into account.

emission would not be brighter than $m_{app} = 22$ mag in any optical bands after ≈ 2 days unless the event occurs within ~ 40 Mpc.

The HK-band emission brighter than -11 mag could last even for a week for both models. In particular, the HK-band emission is as bright as in that observed in GW170817 for ≈ 7–10 days. This is also the case for the emission observed from the equatorial direction. Thus, the HK-band emission would be brighter than $m_{app} = 22$ mag and could be observed by 4 m class telescopes, such as VISTA (Dalton et al. 2006), even for the prompt-collapse cases if the distance to the event is the same as in GW170817 (~ 40 Mpc).

6.2. SMNS Cases (Accelerated Ejecta)

Figure 15 shows the $grizJHK$ light curves for the SMNS models with highly accelerated ejecta. For the SMNS models, bright peak luminosity for the early phase is realized due to the short diffusion timescale associated with the high velocity of the post-merger ejecta. For both SMNS models (SMNS_DYN0.01 and SMNS_DYN0.003), the riz-band emission in the polar region is brighter than that observed in GW170817 by 1–2 mag for $t \lesssim 1$–3 days. Meanwhile, the brightness of those light curves becomes fainter after 1–3 days, and particularly, the g-band emission is always fainter than that in GW170817 after ≈ 0.7 day. In addition, the $griz$-band light emission after $t \gtrsim 2$ days is always fainter than that of the fiducial model, though the post-merger ejecta masses of SMNS_DYN0.01 and SMNS_DYN0.003 are larger than the fiducial case. This implies that a rapid follow-up observation is crucial to find this type of kilonovae and to determine the ejecta properties from the light curves if the ejecta is highly accelerated (Arcavi 2018; Matsumoto et al. 2018).

The same features are also found in the JHK-band light curves. The JHK-band emission is brighter for $\lesssim 3$ days, but it declines much faster than that observed in GW170817 or that of the fiducial model. The JHK-band emission is brighter for the model with larger dynamical ejecta mass (SMNS_DYN0.01), particularly for the late phase ($t \lesssim 4$ days), but it is fainter than that observed in GW170817. Indeed, we find that the post-merger ejecta more massive than $0.1 M_\odot$ is needed for the JHK-band emission to be as bright as that observed in GW170817 for the late phase

($t \gtrsim 6$ days) in the presence of ejecta acceleration. Thus, these results indicate that the faint emission observed for $t \gtrsim 5$ days does not always imply small ejecta mass, and the data points in early phase ($t \gtrsim 3$ days) are crucial to estimate the ejecta properties from the observation.

The clear difference among the SMNS models and the fiducial model is also found in the optical light curves observed from the equatorial direction. The SMNS models with highly accelerated ejecta exhibit brighter iz-band emission than that of the fiducial model, and it is as bright as that observed in GW170817 for $t \approx 1$–2 days. This reflects the fact that optical photons emitted from the high-velocity part of the post-merger ejecta are less absorbed by the dynamical ejecta because the column density measured from the equatorial direction is small.

6.3. BH–NS Cases (NS Tidal Disruption Cases)

Figure 16 shows $grizJHK$ light curves for the BH–NS ejecta models for which the NS is supposed to be tidally disrupted. As is expected from the presence of massive and highly lanthanide-rich dynamical ejecta, the BH–NS ejecta models show bright emission, particularly in the JHK-band. The $izJHK$-band emission observed from the polar direction is much brighter than that in GW170817, while the $griz$-band emission is as bright as that in GW170817. In particular, the BH–NS ejecta model with $0.02 M_\odot$ post-merger ejecta coincidentally reproduces the gr-band data points of GW170817. This implies that kilonovae of BH–NS mergers could be as bright as in GW170817 in the optical wavelengths, but at the same time the emission in the JHK-band would be much brighter. Focusing on the models with the same total ejecta mass (HMNS_YL and BHNS_A), we found that the kilonova of the BH–NS model is always brighter in all the $grizJHK$ bands than that of the NS–NS ejecta model with lanthanide-rich post-merger ejecta. This is due to higher thermalization efficiency of the dynamical ejecta resulting from its higher density profile, while the absence of dynamical ejecta in the polar region for the BH–NS case would also be the reason for the difference in the optical light curves. This indicates that the ejecta mass could be overestimated if the kilonova model for NS–NS is employed for a kilonova from BH–NS.

The optical light curves of BHNS_A and BHNS_B are dominated by the emission from the post-merger ejecta. Indeed, the model with larger post-merger ejecta mass (BHNS_B) and the model only with dynamical ejecta (BHNS_DYN) show slightly brighter and significantly fainter optical emission than that of BHNS_A, respectively. This implies that the presence of the post-merger ejecta also has a large impact on the optical light curves for BH–NS cases and the difference in the post-merger ejecta mass would be reflected in the observed optical light curves, particularly in the gr-band. Meanwhile, the BHNS_A and BHNS_B show approximately the same brightness of iz-band light curves, in spite of the fact that the masses of dynamical and post-merger ejecta for those models are different. BHNS_B and BHNS_DYN also show approximately the same brightness of K-band light curves. This implies that only the light curve in the specific band filter, particularly in the infrared bands, would degenerate with respect to the ejecta mass. Thus, simultaneous observations in the several bands are crucial to estimate the ejecta mass.

As in the other models, the $griz$-band emission observed from the equatorial direction is suppressed due to the presence of dynamical ejecta. However, it is still as bright as that of the NS–NS ejecta model with low-Y_e post-merger ejecta observed
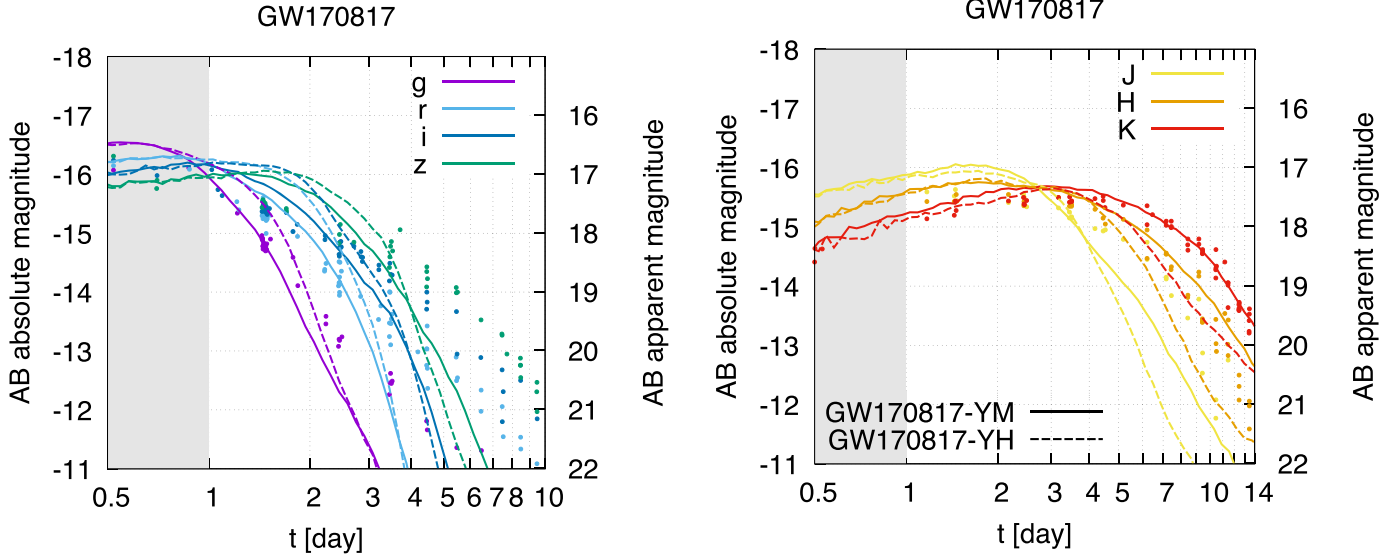
Figure 12. The *grizJHK*-band light curves observed from the polar direction for the models which approximately reproduce the observed peak brightness of GW170817. The solid and dashed curves denote the models with mildly lanthanide-rich (`GW170817_YM`, $X_{\rm pm,lan} \approx 0.025$) and lanthanide-free (`GW170817_YH`, $X_{\rm pm,lan} \ll 10^{-3}$) post-merger ejecta, respectively. light curves observed from $0° \leqslant \theta < 20°$ and $20° \leqslant \theta < 28°$ are shown for the model with mildly lanthanide-rich (`GW170817_YM`) and lanthanide-free (`GW170817_YH`) post-merger ejecta, respectively. For reference, we also plot the data points of GW170817 (Villar et al. 2017).
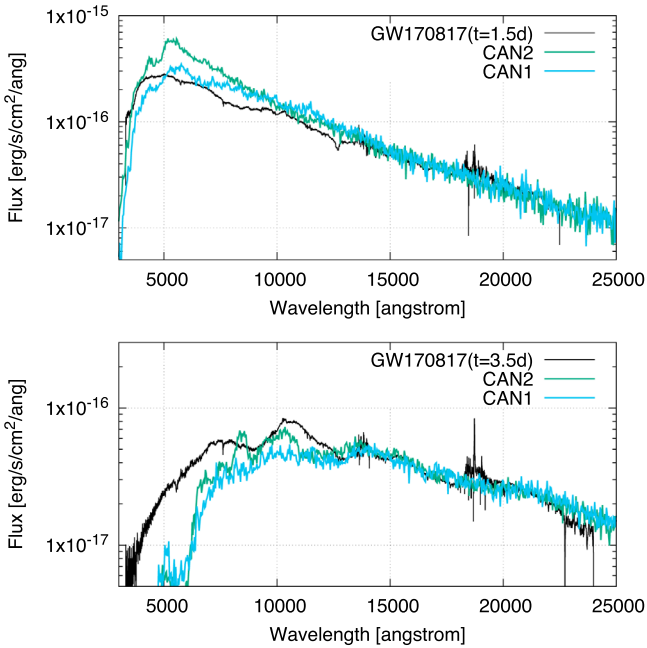
Figure 13. The spectra at $t \approx 1.5$ days (top panel) and $t \approx 3.5$ days (bottom panel) observed from the polar direction for the models which approximately reproduce the observed peak brightness of GW170817. The blue and green curves denote the models with mildly lanthanide-rich (`GW170817_YM`) and lanthanide-free (`GW170817_YH`) post-merger ejecta, respectively. The black curves denotes the spectra of GW170817 taken with VLT/X-Shooter (Pian et al. 2017; Smartt et al. 2017). Spectra observed from $0° \leqslant \theta < 20°$ and $20° \leqslant \theta < 28°$ are shown for the model with mildly lanthanide-rich (`GW170817_YM`) and lanthanide-free (`GW170817_YH`) post-merger ejecta, respectively.

from the polar direction, while the *z*-band emission is as bright as in GW170817. We note that the emission observed from the equatorial direction is dominated by the emission from the dynamical ejecta. Indeed, the BH–NS ejecta models with the same mass of dynamical ejecta (`BHNS_A` and `BHNS_DYN`)

exhibit approximately the same brightness of light curves. The model with smaller dynamical ejecta mass (`BHNS_B`) shows fainter emission. Thus, both optical and infrared emission for BH–NS mergers could be as bright as that of NS–NS mergers, even from the equatorial direction if dynamical ejecta with sufficiently large mass (say $\gtrsim 0.02\,M_\odot$) is launched.

Before closing this subsection, we note that the ejecta mass for BH–NS mergers could have a large variety depending on the binary parameters. For example, a massive post-merger ejecta ($\gtrsim 0.01$–$0.05\,M_\odot$) associated with only small amount of dynamical ejecta ($\lesssim 0.001\,M_\odot$) would be launched for a BH–NS merger if the mass ratio of the BH to the NS is close to unity (Foucart et al. 2019). For such a case, the kilonova light curves would be similar to those for `PM_YL`. The peak brightness observed from the polar direction would be fainter than that for BH–NS mergers with substantial amount of dynamical ejecta (`BHNS_A` and `BHNS_B`), due to the absence of the radiative transfer effect in the multiple ejecta components, while the peak brightness observed from the equatorial direction would be similar (see the results of `PM_YL` in Figures 17 and 18). It should be also noted that eject mass for BH–NS mergers could be quite small ($\lesssim 0.001\,M_\odot$) if NS is only weakly disrupted before the merger. For such a case, the light curves are likely to be similar to those for NS–NS mergers collapsing promptly to a BH.

6.4. Comparison Among Various Models

As a summary for the variety in kilonova light curves, Figures 17 and 18 compare the peak magnitude and time of peak in the *iJK*-band observed from the polar direction ($0° \leqslant \theta \leqslant 20°$) and equatorial direction ($86° \leqslant \theta \leqslant 90°$), respectively, among various kilonova models. Here, we note that the peak magnitude is practically defined as the brightest magnitude for $t \geqslant 1$ day due to the limitation in our calculation.

The peak magnitude in the *K*-band shows a rich variety in both brightness and time of peak among the models. In particular, the models of the same category (SMNS, HMNS, and Prompt
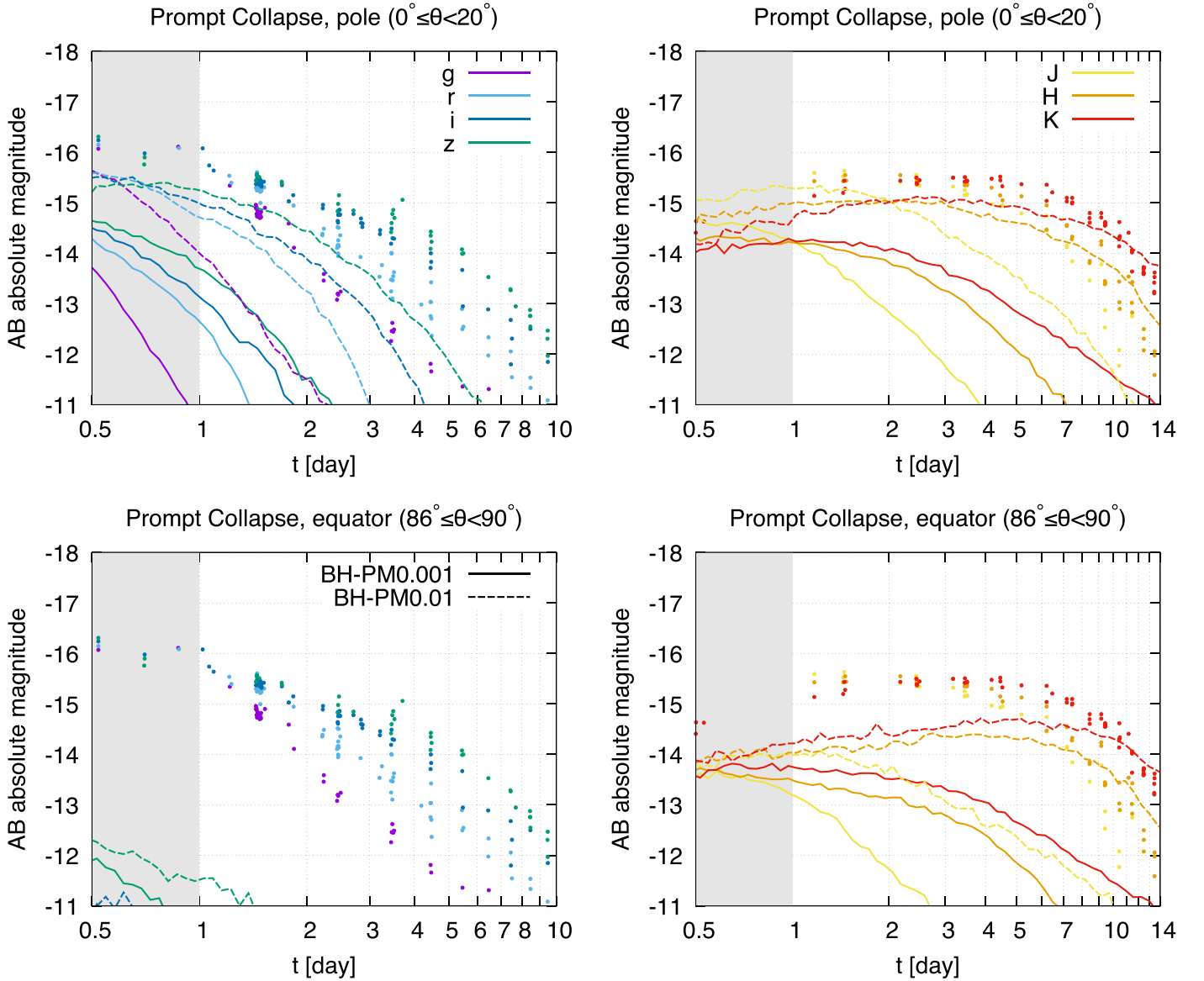
Figure 14. The *grizJHK*-band light curves for prompt-collapse ejecta models. The solid and dashed curves denote the small post-merger ejecta mass model (`BH_PM0.001`; $M_{pm} = 0.001\ M_\odot$) and relatively large post-merger ejecta mass model (`BH_PM0.01`; $M_{pm} = 0.01\ M_\odot$), respectively. For reference, we also plot the data points of GW170817 (Villar et al. 2017).

collapse) are approximately clustered in the same region of peak brightness and time of peak; for the polar emission, the HMNS models (the models referred to as `HMNS_...`) are in the region of peak brightness ≈ -16.5–15.5 mag and time of peak ≈ 2–5 days, the SMNS models (`SMNS_DYN0.01` and `SMNS_DYN0.003`) in ≈ -16.5 mag and $\lesssim 2$ days, the prompt-collapse models (`BH_PM0.001` and `BH_PM0.01`) in $\gtrsim -15$ mag and $\lesssim 2.5$ days. The peak magnitude and time of peak observed from the equatorial direction also show approximately the same qualitative feature, while the brightness at the peak is typically fainter by ≈ 0.5 mag than that observed from the polar direction. This indicates that we may be able to infer the type of the central engine for kilonovae by observing the peak of the light curves in the infrared bands.

The peak magnitudes in the *iJ*-band for the polar emission agree with each other within ≈ 0.5 mag among the various models, except for the prompt collapse (`BH_PM0.001` and `BH_PM0.01`) and SMNS (accelerated ejecta) models (`SMNS_DYN0.01` and

`SMNS_DYN0.003`). The results of the prompt collapse (`BH_PM0.001` and `BH_PM0.01`) and SMNS (accelerated ejecta) models (`SMNS_DYN0.01` and `SMNS_DYN0.003`) show brighter and fainter peak brightness in the *i* or *J*-band than the other models by more than 1 mag, respectively. The peak magnitudes in the *J*-band for the equatorial emission also show approximately the same qualitative feature. This indicates that we may be able to distinguish the prompt collapse and SMNS cases by the other cases from the observation of the peak brightness in the near-infrared bands.

We note that the peak magnitude and time of peak for a BH–NS merger would have diversity, which reflects the large variety of ejecta mass depending on the binary parameters. For example, the peak emission would be faint and the light curves would decline quickly, as is the case for the prompt-collapse models if NS tidal disruption only weakly occurs and only small amount of ejecta is launched. Thus, we should note that a kilonova for a BH–NS merger could also exhibit peak
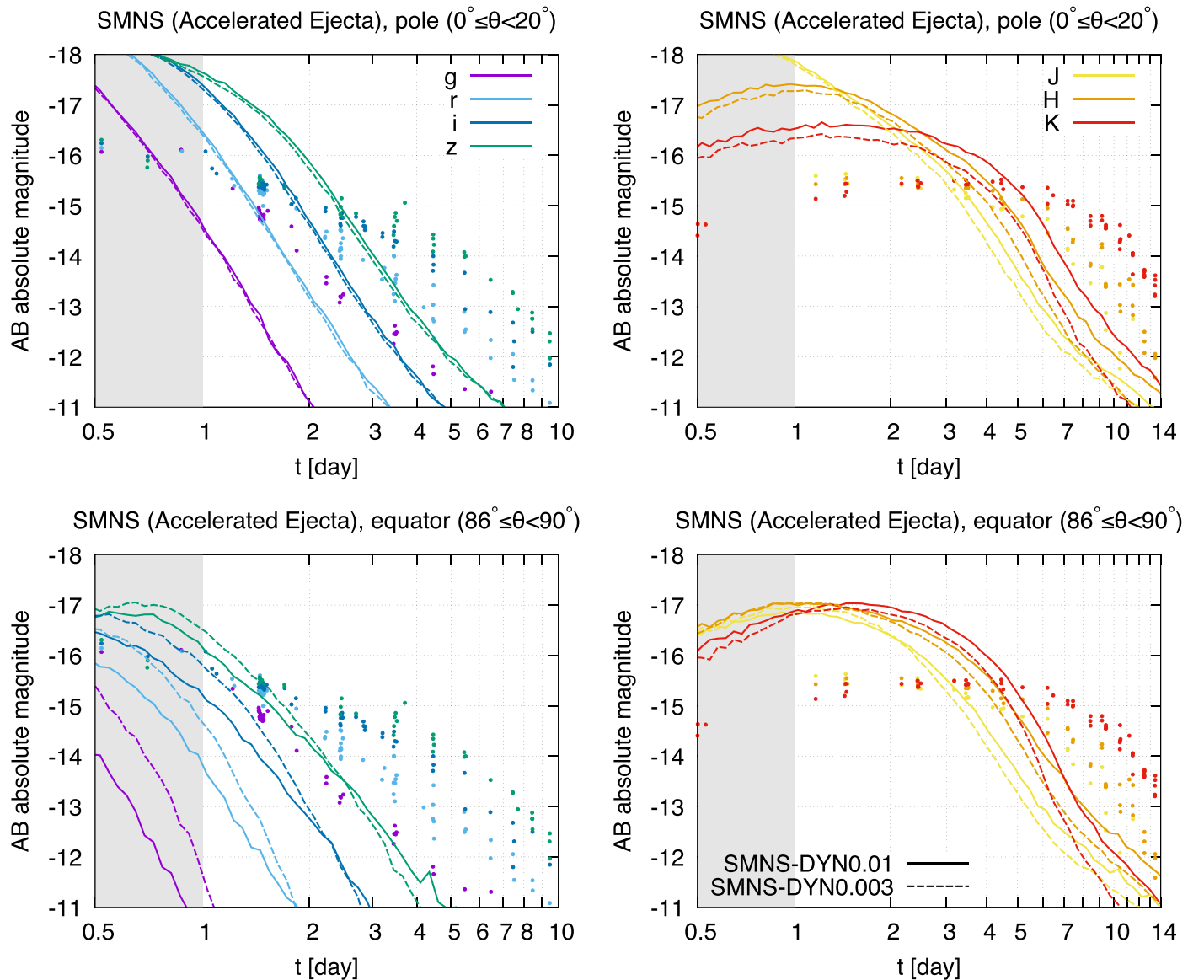
Figure 15. The *grizJHK*-band light curves for the SMNS models with highly accelerated ejecta. The solid and dashed curves denote the models with 0.01 $M_\odot$ dynamical ejecta (`SMNS_DYN0.01`) and with 0.003 $M_\odot$ dynamical ejecta (`SMNS_DYN0.003`), respectively. For reference, we also plot the data points of GW170817 (Villar et al. 2017).

brightness and time of peak similar to those of the prompt-collapse or HMNS cases.

7. Summary

We performed radiative transfer simulations for kilonova light curves for a variety of ejecta profiles suggested by latest numerical simulations. The radiative transfer simulations were performed by employing a new line list that was obtained by systematic atomic structure calculations for all of the *r*-process elements (Tanaka et al. 2019).

We demonstrated the strong effect of the radiative transfer of photons in the multiple ejecta components on the resulting light curve of kilonovae and we clarified the dependence of the light curves on the ejecta parameters. We showed that the brightness of the optical light curves observed in the polar direction could be enhanced by 50%–100% in the presence of optically thick dynamical ejecta concentrated near the equatorial plane, due to the preferential diffusion to the polar direction. This indicates

that the ejecta mass could be overestimated by a factor of ∼2 if one fails to take this effect into account. We found that this enhancement of the optical emission, particularly for the early phase of $t \lesssim 2$ days, depends only weakly on the dynamical ejecta mass as long as $M_d \geqslant 0.001 M_\odot$. In addition, significant angular dependence of the optical emission was found in the presence of dynamical ejecta with $M_d \geqslant 0.001 M_\odot$. Indeed, we found that the optical emission observed from the equatorial direction would be fainter by more than 3 mag than that observed from the polar direction for such a case. Since numerical-relativity simulations with a variety of binary parameters show that the dynamical ejecta with its mass larger than $0.001 M_\odot$ are often driven (Bauswein et al. 2013; Hotokezaka et al. 2013; Radice et al. 2016; Sekiguchi et al. 2016; Bovard et al. 2017; Dietrich et al. 2017), taking the effect of this enhancement in the optical bands due to the preferential diffusion as well as the angular dependence of the light curves into account would be indispensable for estimating the ejecta mass.
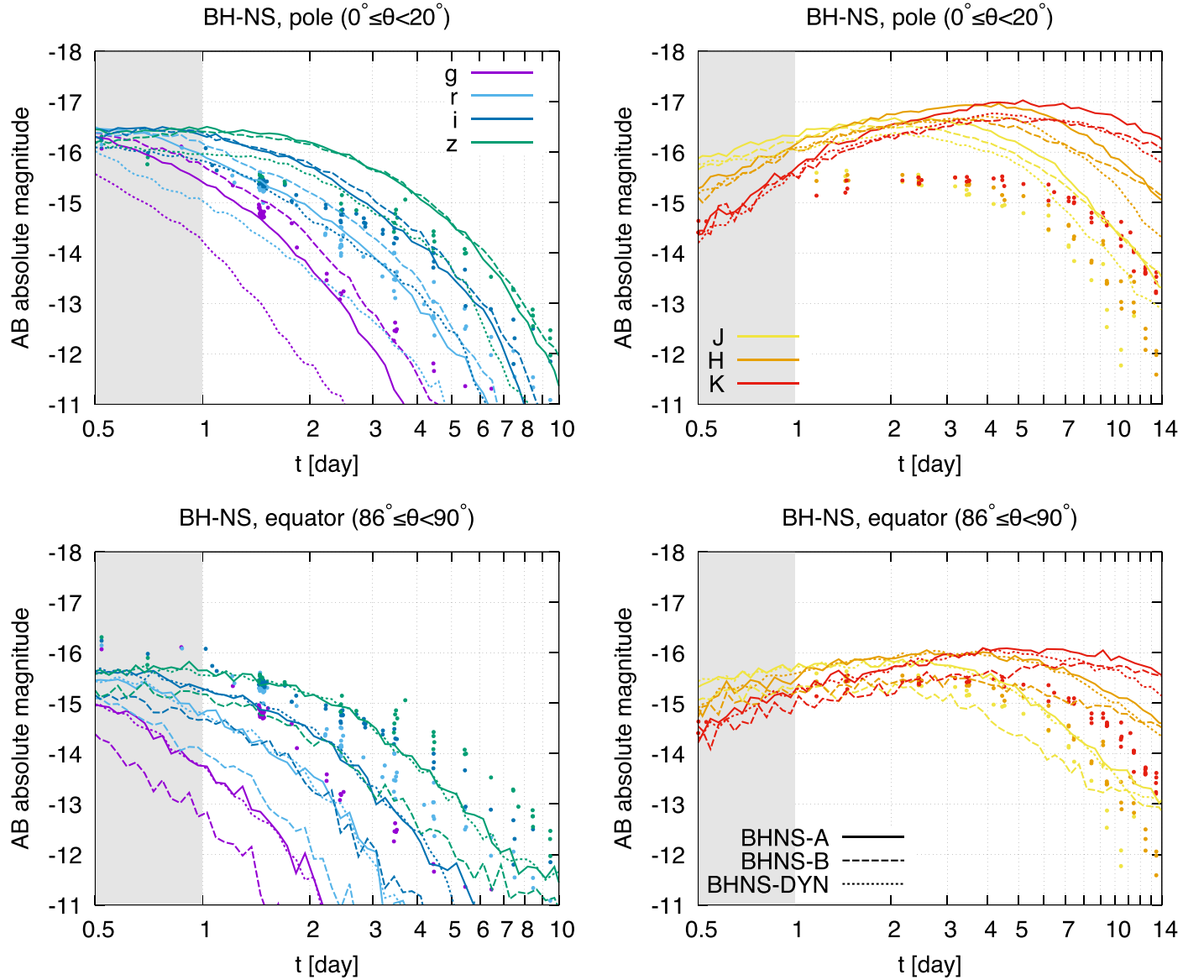
Figure 16. The *grizJHK*-band light curves for the BH–NS ejecta models. The solid curves denote the result of the BH–NS ejecta model with 0.02 $M_\odot$ post-merger ejecta and 0.02 $M_\odot$ dynamical ejecta (BHNS_A). Dashed curves denote the results of the BH–NS ejecta models (BHNS_B) with more massive post-merger ejecta (0.04 $M_\odot$) and less massive dynamical ejecta (0.01 $M_\odot$). Dotted curves denote the results for the model only with dynamical ejecta (BHNS_DYN). For reference, we also plot the data points of GW170817 (Villar et al. 2017).

We showed that the infrared brightness is also enhanced by the emission from the post-merger ejecta reprocessed in the dynamical ejecta. In addition, we showed that the infrared emission is enhanced by emission from the post-merger ejecta, particularly for the presence of lanthanide. This implies that the infrared light curves depend not only on the mass and velocity of the dynamical ejecta but also significantly on the mass, velocity, and the lanthanide fraction of the post-merger ejecta, and that the infrared light curves have strong degeneracy with respect to the ejecta parameters. Thus, if we wish to extract the physical information of the ejecta, then it is crucial to observe the light curves in a wide range of wavelengths and consider the effect of the radiative transfer of photons in the multiple ejecta components.

Based on the parameter dependence of the light curves studied in this work, we searched for the ejecta parameters that can interpret the optical and infrared light curves of the EM counterpart observed in GW170817. We showed that the

lanthanide-free post-merger ejecta ($X_{\rm pm,lan} \ll 10^{-3}$) is not necessarily required to interpret the peak brightness in the optical bands observed in GW170817 (Kasen et al. 2017; Perego et al. 2017). Indeed, we showed that mildly lanthanide-rich post-merger ejecta ($X_{\rm pm,lan} \approx 0.025$) reproduces the peak brightness in the optical bands because of the preferential diffusion to the polar region, and it reproduces the observed infrared light curves for the late phase of $\lesssim 7$ days for our setup. Furthermore, we found that the spectra become more featureless by employing lanthanide-rich post-merger ejecta than by employing lanthanide-free ejecta, which is consistent with the observation. This suggests that featureless spectra observed in GW170817 might be explained by mildly lanthanide-rich ejecta with $\lesssim 0.1c$ while lanthanide-free ejecta with high velocity $\lesssim 0.3c$ is often claimed to be necessary (e.g., Kilpatrick et al. 2017; McCully et al. 2017; Nicholl et al. 2017; Shappee et al. 2017; Tanaka et al. 2019). Meanwhile, we found that it is not easy to reproduce the optical brightness for
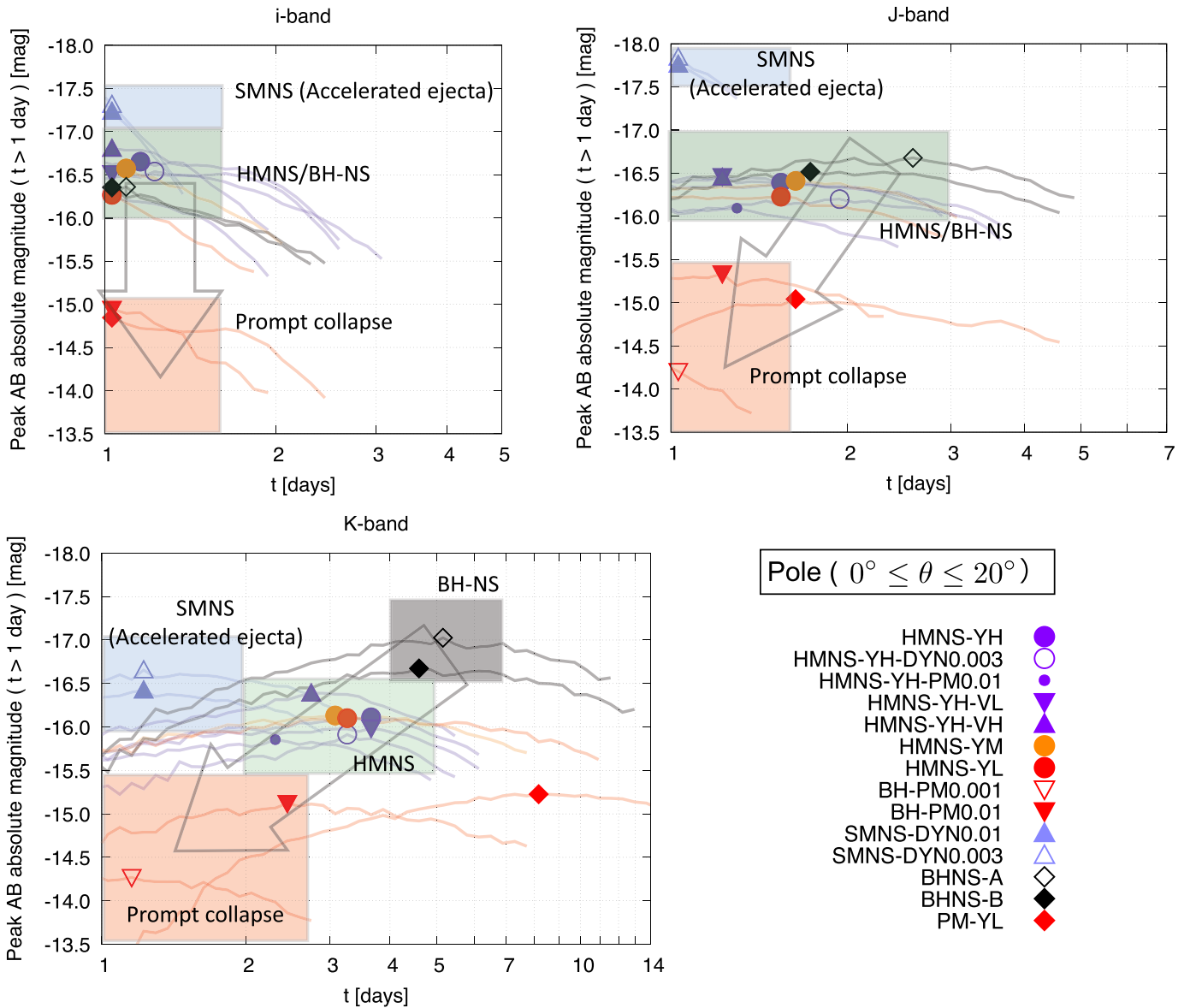
Figure 17. Comparison of the peak magnitude (the brightest magnitude for $t \geqslant 1$ day) in the iJK-band observed from the polar direction ($0° \leqslant \theta \leqslant 20°$) among various kilonova models. Each point in the plot shows the time of peak and its magnitude for each kilonova model. The brightness of these light curves is within ≈ 1 mag and ≈ 0.5 mag from the peak magnitude and is shown in the plots for the i-band and the JK-band, respectively. The blue, green, red, and black regions denote the regions in which the peak brightness and time of peak approximately cluster for the SMNS, HMNS, prompt collapse, and BH–NS models (NS tidal disruption cases), respectively. We note that the ejecta mass for BH–NS mergers could have a large variety depending on the binary parameters, and the peak brightness and time of peak would become faint and shifted toward the early phase, respectively, (toward the direction of arrows in the figure) for a small amount of ejecta.

the late phase ($t \gtrsim 2$ days) in our setups of ejecta model. This suggests that additional ejecta components may be needed to interpret the observed optical brightness of the light curves for the late phase. Alternatively, the different function of the heating rate and taking the non-LTE effect into account could also modify the results, and thus further investigation is required to achieve conclusive statements.

We found that the optical emission of kilonova for the prompt collapse of NS–NS mergers to a BH would be much fainter than that observed in GW170817 due to small ejecta masses. However, if the event occurs at the same distance as in GW170817 and the post-merger ejecta is as massive as $0.01 M_\odot$, then the riz-band emission observed from the polar direction may still be brighter than $m_{app} = 20$ mag for

$t \lesssim 3$ days. In particular, for this case, the JHK-band emission would be as bright as in GW170817.

For the case where the ejecta is accelerated by an energy injection from the merger remnant, we found that the optical and infrared emission could be brighter by 1–2 mag than that observed in GW170817 for $t \lesssim 4$ days and for $t \lesssim 7$ days, respectively, due to the short diffusion timescale associated with the high velocity of the post-merger ejecta. We also found that it declines much faster than that observed in GW170817. In addition, the suppression of the optical emission observed from the equatorial direction is less significant for the case where the post-merger ejecta is highly accelerated than that in the fiducial case. This indicates that the presence of a high-velocity ejecta component may be confirmed from the optical
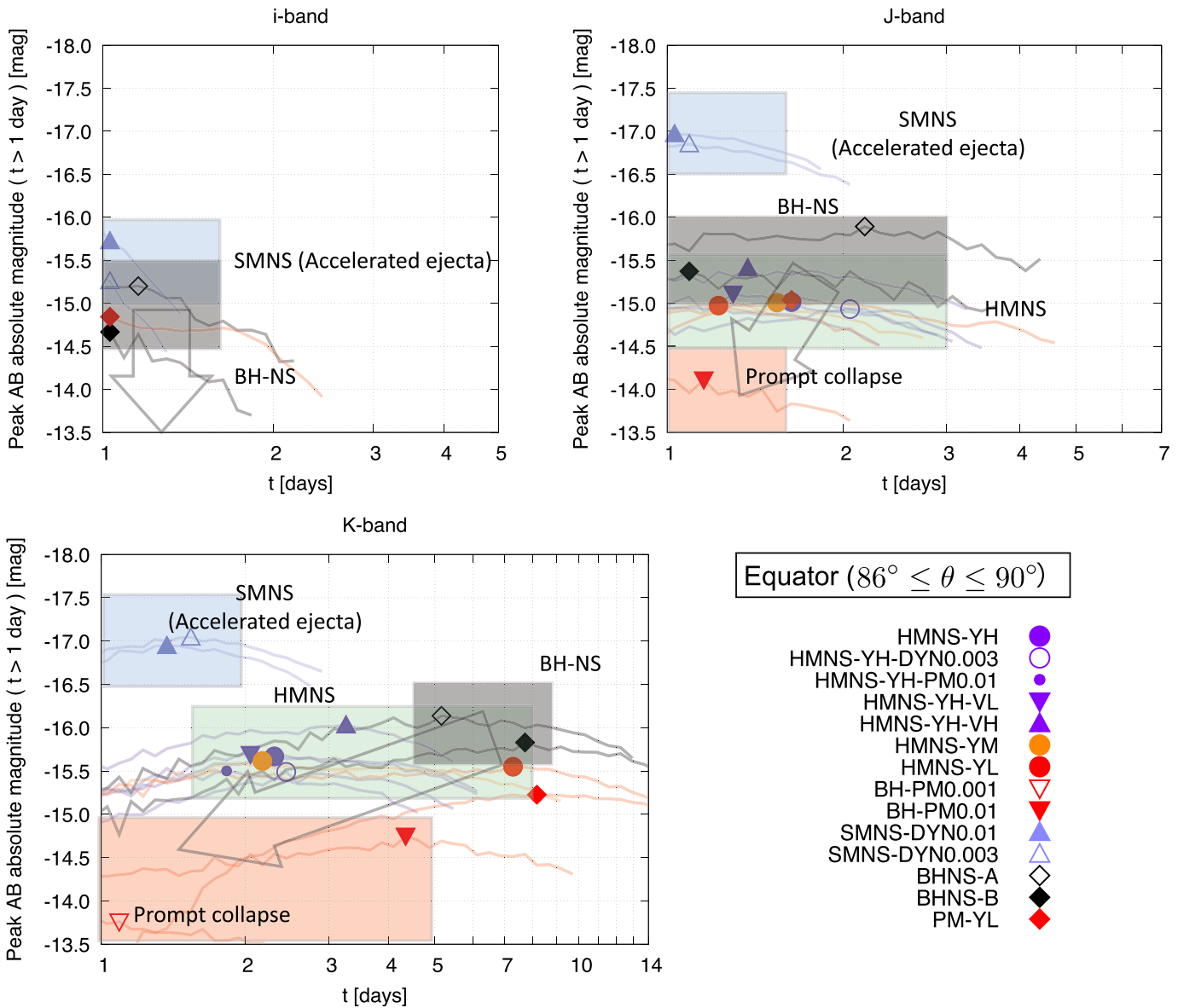
Figure 18. The same as Figure 17 but for the equatorial direction ($86° \leqslant \theta \leqslant 90°$).

light curves for the case where the edge-on observation is suggested by the GW data analysis.

We also studied kilonova light curves for BH–NS mergers that result in NS tidal disruption. We found that the optical emission could be as bright as, or even brighter than that observed in GW170817 if substantial mass ($\gtrsim 0.02\,M_\odot$) of post-merger ejecta is ejected, although we should note that the ejecta mass could have a large variety depending on the binary parameters. For these high ejecta mass cases, we showed that the infrared emission would be brighter by 1–2 mag than that observed in GW170817 due to the large amount of lanthanide-rich ejecta, and thus we may be able to distinguish the NS–NS from the BH–NS merger. Meanwhile, the similar light curves could be realized in a specific band even if the ejecta mass is different. This indicates that the simultaneous observation in the multiple wavelengths is crucial for the ejecta mass estimation. We also note that eject mass for BH–NS mergers could be quite small ($\lesssim 0.001\,M_\odot$) if NS is only weakly disrupted before the merger. For this case, the light curves are

likely to be similar to those for NS–NS mergers collapsing promptly to a BH. We also note that ejecta would not launched for BH–NS mergers if NS tidal disruption does not occur before the merger. In this case, the kilonova would not associate with the gravitational wave event.

We showed that the difference in the ejecta properties would be imprinted in the differences in the peak brightness and time of peak of kilonovae (Figures 17 and 18). This indicates that we may be able to distinguish the different merger evolution by observations of the peak in the light curves. Consequently, it is crucial to obtain multi-color data from optical to infrared because there is a degeneracy in the peak brightness and peak time in some specific filters whose wavelengths are close to each other. We note that more systematic studies varying the ejecta parameters and also the assumptions for calculations, such as the model for the heating rates, would be necessary to quantitatively understand how well we can distinguish models, which is beyond the scope of this paper.
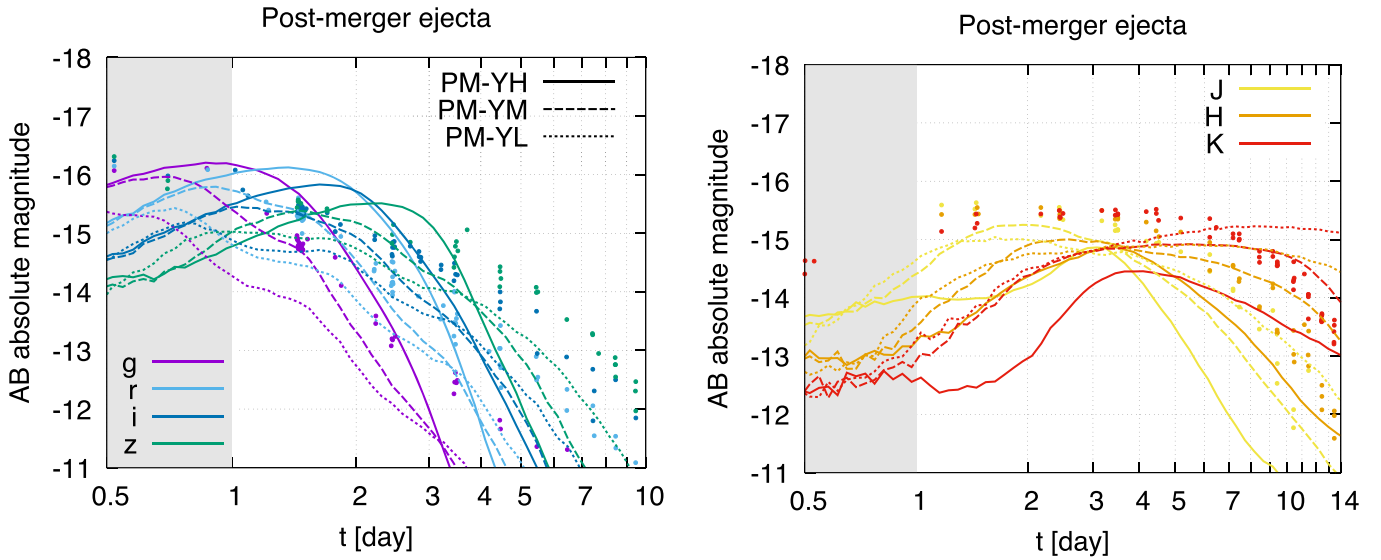
Figure 19. The *grizJHK*-band light curves for the models only with the post-merger ejecta. The solid, dashed, and dotted curves denote the light curves for the models with flat Y_e distributions in 0.3–0.4 (PM_YH, $X_{pm,lan} \approx 0.025$), 0.2–0.4 (PM_YM $X_{pm,lan} \ll 10^{-3}$), and 0.1–0.3 (PM_YL $X_{pm,lan} \approx 0.14$), respectively. For reference, we also plot the data points of GW170817 (Villar et al. 2017).

Appendix A
Light Curves of Each Ejecta Component

In this section, we show the results and their basic properties of the light curves obtained by the radiative transfer simulations for each ejecta component.

A.1. Post-merger Ejecta

Figure 19 shows the *grizJHK*-band light curves of the post-merger ejecta models with different Y_e distributions. The dependence on the Y_e distribution is basically the same as is found in the Section 4. The *griz*-band emission becomes faint and the slopes of decline become shallow as the lanthanide fraction of the post-merger ejecta increases (i.e., as the fraction of low-Y_e components increases).

The *JHK*-band emission for $t \gtrsim 3.5$ days becomes bright monotonically as the lanthanide fraction of the post-merger ejecta increases, while the brightness of the *JHK*-band light curves for $t \lesssim 3.5$ days saturates for the case that the lanthanide fraction is higher than that of PM_YM. In particular, the *HK*-band emission for the early phase ($t \approx 1$ day) is fainter than those peak magnitudes by ≈ 1 mag. This happens because the time of peak magnitudes typically delays as the lanthanide fraction of the post-merger ejecta increases due to longer diffusion timescale.

For $t \leqslant 2$–3 days, the *griz*-band light curves with lanthanide-free post-merger ejecta (PM_YH) and with mildly lanthanide-rich post-merger ejecta (PM_YM) are broadly consistent with the observed data points in GW170817. In contrast, we find that those with highly lanthanide-rich post-merger ejecta (PM_YL) are fainter than the data in GW170817.

A.2. Dynamical Ejecta

Figure 20 shows the results for the models only with dynamical ejecta of different masses. As is expected, a kilonova is brighter for larger mass. In addition, significant angular dependence is present in the optical light curves due to the non-spherical morphology and their brightness is strongly suppressed when observed from the equatorial direction.

The *JHK*-band emission is brighter than that in the *griz*-band due to high lanthanide fraction of the dynamical ejecta. The *JHK*-band light curves exhibit approximately the same brightness as in the peak ($t \approx 1$ days), and are sustained for a few days. The angular dependence of the *JHK*-band light curves is much weaker than the *griz*-band light curves. Indeed, the *JHK*-band emission observed from the equatorial direction is fainter than that observed from the polar direction only by ≈ 0.5 mag.
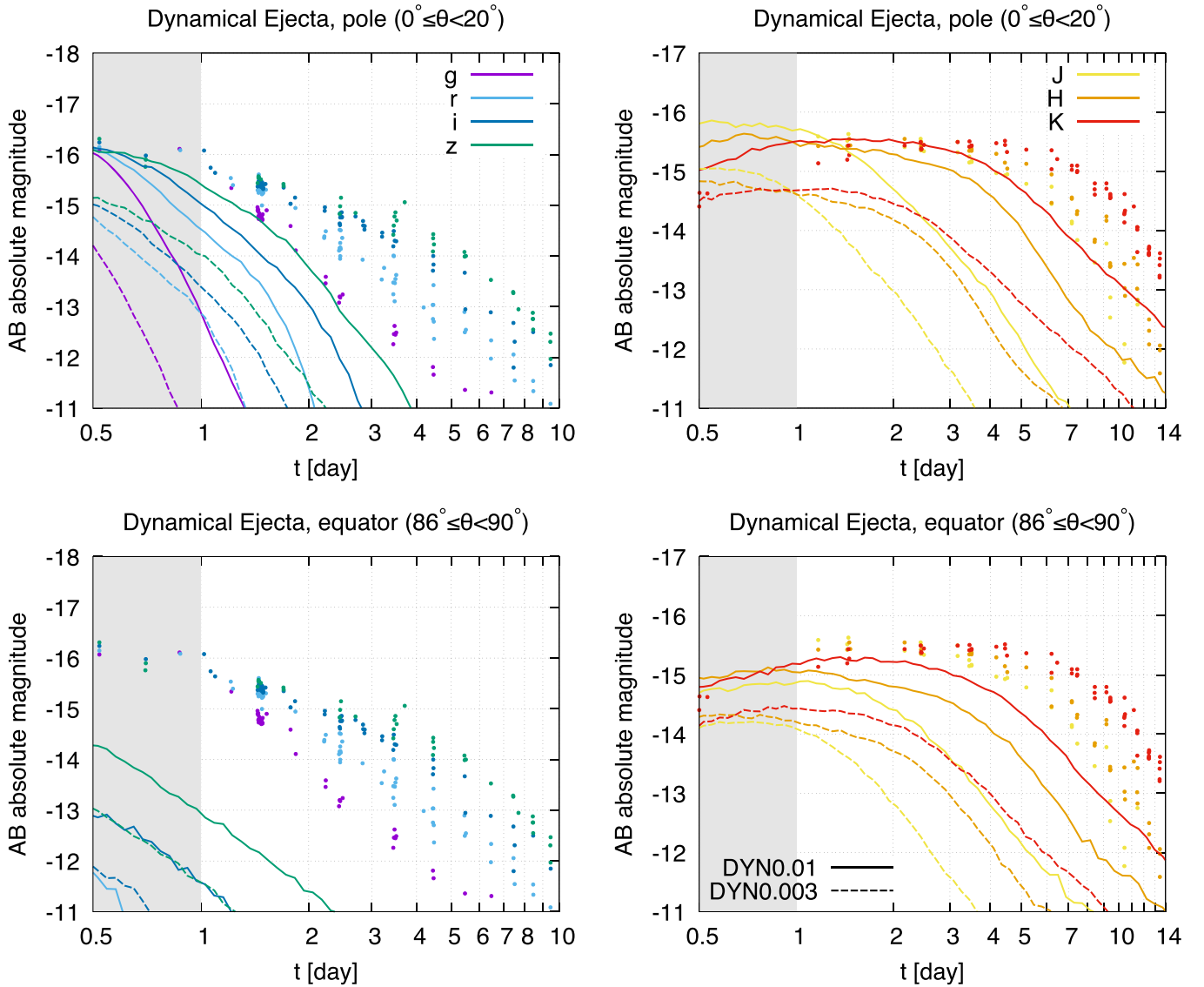
Figure 20. The *grizJHK*-band light curves for the models only with dynamical ejecta. The solid and dashed curves denote the light curves obtained by the models of which dynamical ejecta mass are 0.01 $M_\odot$ (DYN0.01) and 0.003 $M_\odot$ (DYN0.003), respectively. For reference, we also plot the data points of GW170817 (Villar et al. 2017).

Appendix B
Light Curves Observed from $20° \leqslant \theta < 28°$

The GW data analysis infers that GW170817 is observed from $\theta \lesssim 28°$ (Abbott et al. 2017b), while the light curves

observed from $0° \leqslant \theta < 20°$ are only shown in Section 4. Thus, here, we plot the *grizJHK*-band light curves observed from $20° \leqslant \theta < 28°$ as complementary information to enable the readers to make a comparison to the observed data (see Figure 21).
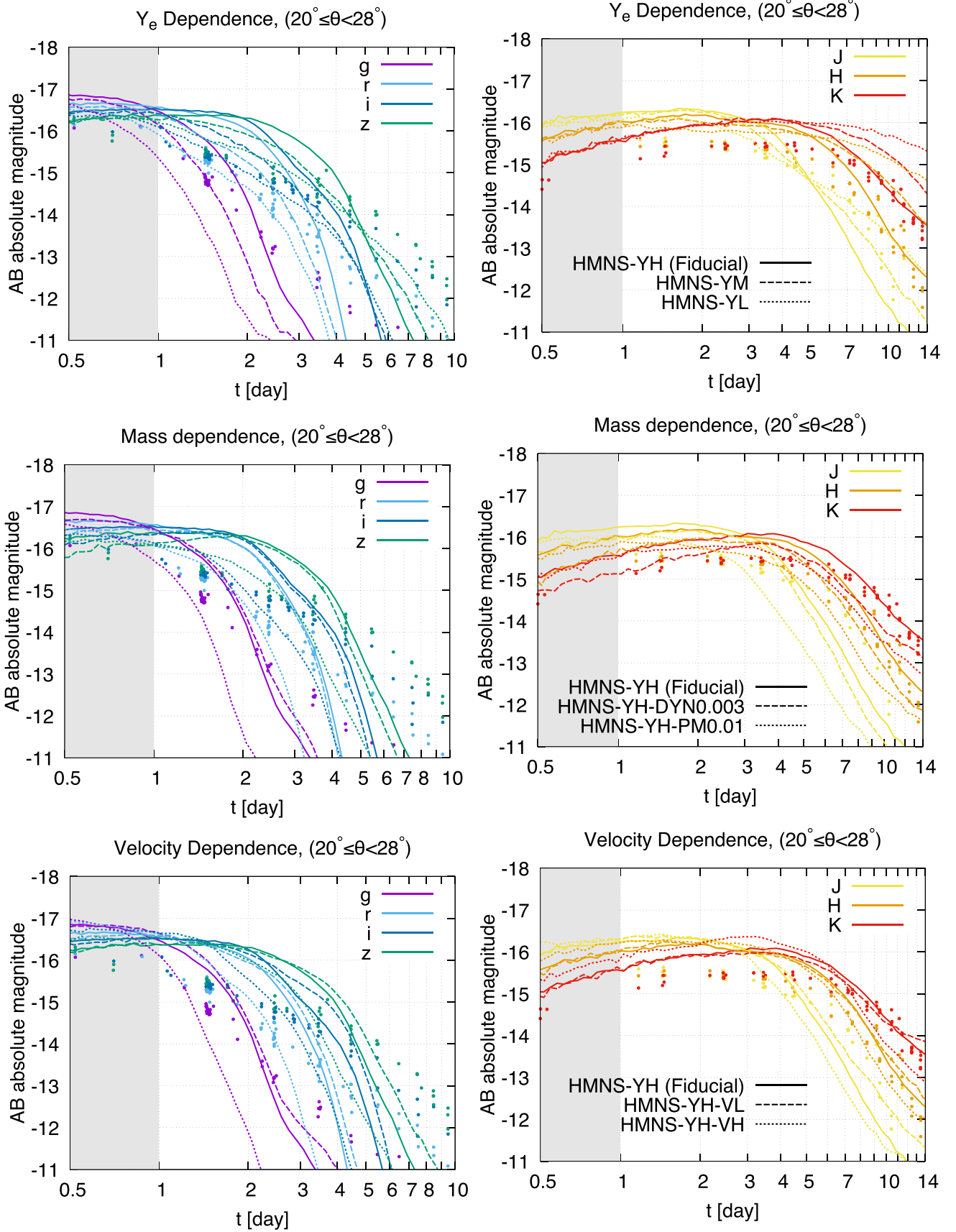
Figure 21. The *grizJHK*-band light curves observed from $20° \leqslant \theta < 28°$ for the models shown in Section 4. For reference, we also plot the data points of GW170817 (Villar et al. 2017).

Appendix C
Contribution of Fission Fragments to the Heating Rate

The contribution of the fission fragments to the heating rate is highly uncertain (e.g., Wanajo 2018). To check how such uncertainty affects the results in this paper, we compare the light curves with and without considering the contribution of fission fragments to the heating rate for several models studied in this paper.

Figure 22 compares the *giJK*-band light curves with (solid curves) and without (dotted curves) the contribution of fission fragments to the heating rate for the BH–NS ejecta models (BHNS_A and BHNS_B). The kilonova emission for the models without fission fragments is fainter than that with fission fragments by more than ≈0.5 mag. The difference is more significant for the model with larger dynamical ejecta (BHNS_A) than the model with

less dynamical ejecta (BHNS_B), which reflects that uncertainty in fission fragments has a large impact on the emission, particularly from the dynamical ejecta.

Figure 23 is the same as Figure 22 but for the HMNS ejecta models (HMNS_YH and HMNS_YL). In contrast to the BH–NS ejecta models, the difference in the light curves between the models with and without fission fragments are always smaller than ≈0.5 mag for the HMNS ejecta models, and is approximately absent for the model with the lanthanide-poor post-merger ejecta (HMNS_YH). The reason why the difference in the HMNS ejecta models is less significant than the BH–NS models is that the average Y_e value of the dynamical ejecta is set to higher values for the HMNS ejecta models than the BH–NS ejecta models, and the contribution of fission fragments to the heating rate is less significant. Indeed, the electron fraction of the dynamical ejecta for the HMNS models is widely distributed from 0.1 to 0.3, while that
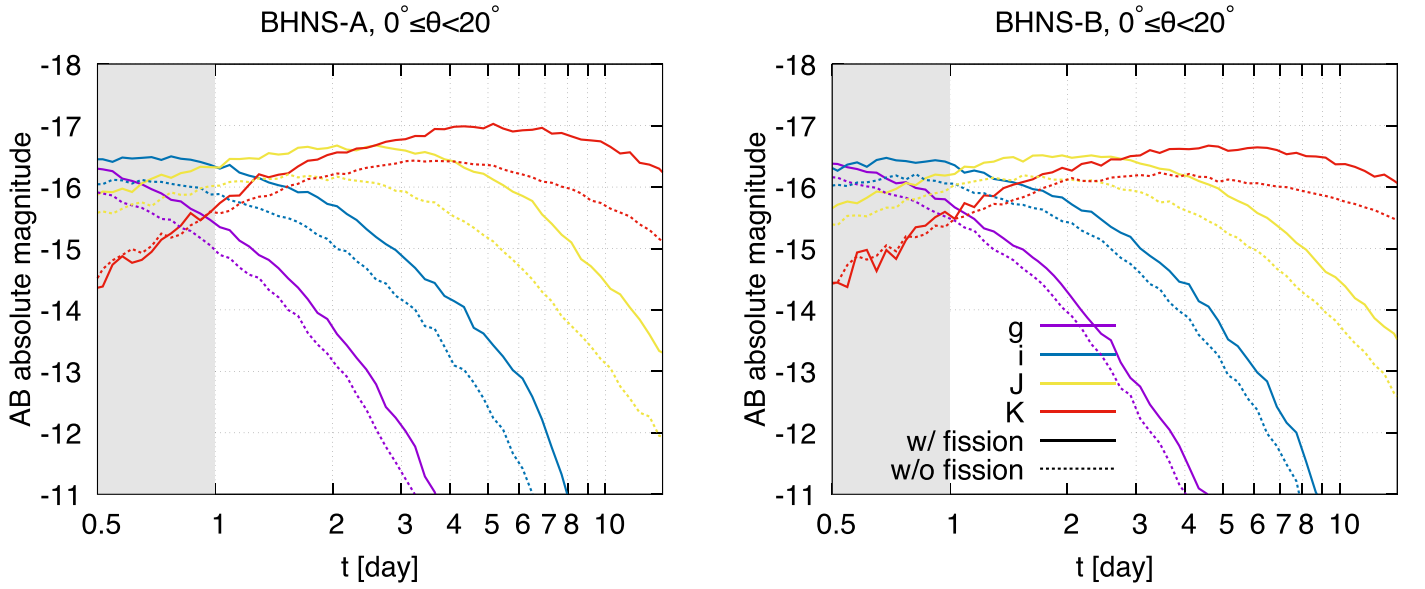

Figure 22. Comparison of the *giJK*-band light curves with (solid curves) and without (dotted curves) the contribution of fission to the heating rate for the BH–NS ejecta models (BHNS_A and BHNS_B).
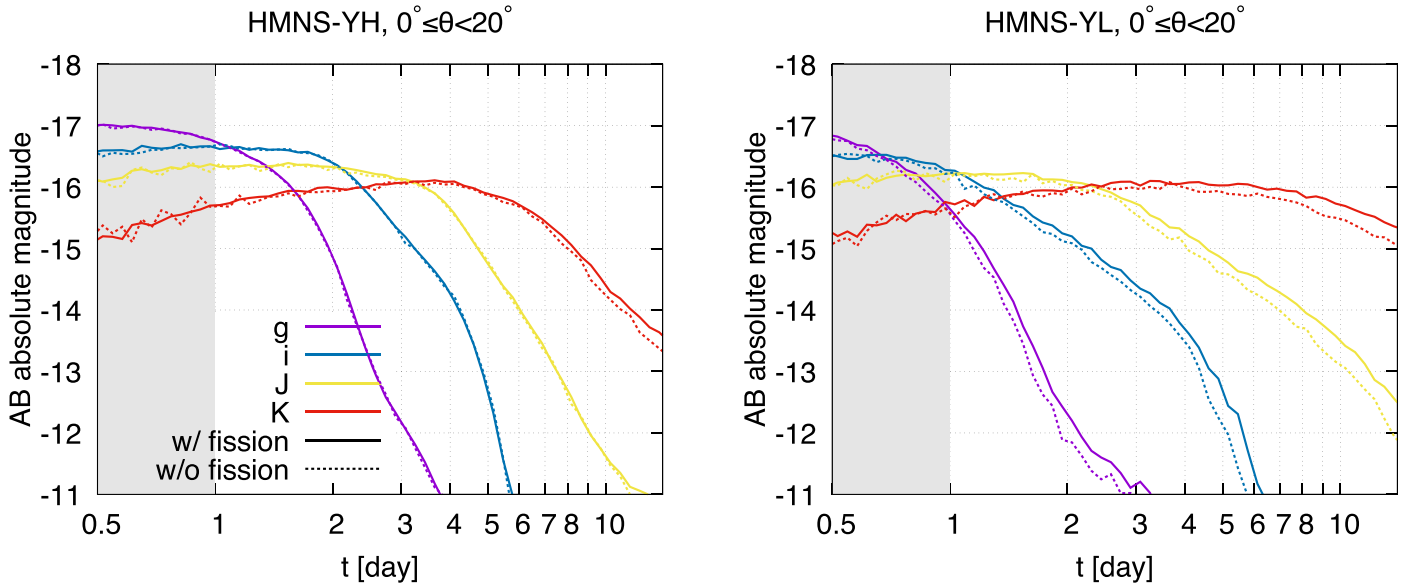

Figure 23. Comparison of the *giJK*-band light curves with (solid curves) and without (dotted curves) the contribution of fission to the heating rate for the HMNS ejecta models (HMNS_YH and HMNS_YL).

of the BH–NS models is set to $\lesssim 0.1$, and the heating is dominated by the contribution from β-decays or α-decays for the former cases. Thus, uncertainty in the contribution of fission fragments to the heating rate has the largest impact on the light curves, particularly for the case where the Y_e value is as low as in the cases of BH–NS mergers (or the prompt-collapse cases of NS–NS mergers).

ORCID iDs

Masaru Shibata ⓘ https://orcid.org/0000-0002-4979-5671
Masaomi Tanaka ⓘ https://orcid.org/0000-0001-8253-6850

References

Abbott, B., Abbott, R., Abbott, T. D., et al. 2017b, PhRvL, 119, 161101
Abbott, B. P., Abbott, R., Abbott, T. D., et al. 2017a, ApJL, 848, L12
Andreoni, I., Ackley, K., Cooke, J., et al. 2017, PASA, 34, e069
Arcavi, I. 2018, ApJL, 855, L23
Arcavi, I., Hosseinzadeh, G., Howell, D. A., et al. 2017, Natur, 551, 64
Ascenzi, S., Coughlin, M. W., Dietrich, T., et al. 2019, MNRAS, 486, 672
Barnes, J., Kasen, D., Wu, M.-R., & Martínez-Pinedo, G. 2016, ApJ, 829, 110
Bauswein, A., Goriely, S., & Janka, H. T. 2013, ApJ, 773, 78
Bellm, E., & Kulkarni, S. 2017, NatAs, 1, 0071
Bovard, L., Martin, D., Guercilena, F., et al. 2017, PhRvD, 96, 124005
Bulla, M. 2019, MNRAS, 489, 5037
Coulter, D. A., Foley, R. J., Kilpatrick, C. D., et al. 2017, Sci, 358, 1556
Cowperthwaite, P. S., Berger, E., Villar, V. A., et al. 2017, ApJL, 848, L17
Dalton, G. B., Caldwell, M., Ward, A. K., et al. 2006, Proc. SPIE, 6269, 62690X
Dessart, L., Ott, C., Burrows, A., Rosswog, S., & Livne, E. 2009, ApJ, 690, 1681
Díaz, M. C., Macri, L. M., Garcia Lambas, D., et al. 2017, ApJL, 848, L29
Dietrich, T., Ujevic, M., Tichy, W., Bernuzzi, S., & Bruegmann, B. 2017, PhRvD, 95, 024029
Drout, M. R., Piro, A. L., Shappee, B. J., et al. 2017, Sci, 358, 1570
Eastman, R. G., & Pinto, P. A. 1993, ApJ, 412, 731
Eichler, D., Livio, M., Piran, T., & Schramm, D. N. 1989, Natur, 340, 126
Etienne, Z. B., Liu, Y. T., Shapiro, S. L., & Baumgarte, T. W. 2009, PhRvD, 79, 044024
Evans, P. A., Cenko, S. B., Kennea, J. A., et al. 2017, Sci, 358, 1565
Fernández, R., Tchekhovskoy, A., Quataert, E., Foucart, F., & Kasen, D. 2019, MNRAS, 482, 3373
Foucart, F., Desai, D., Brege, W., et al. 2017, CQGra, 34, 044002
Foucart, F., Duez, M. D., Kidder, L. E., et al. 2019, PhRvD, 99, 103025
Foucart, F., Haas, R., Duez, M. D., et al. 2016, PhRvD, 93, 044019
Foucart, F., Hinderer, T., & Nissanke, S. 2018, PhRvD, 98, 081501
Fujibayashi, S., Kiuchi, K., Nishimura, N., Sekiguchi, Y., & Shibata, M. 2018, ApJ, 860, 64
Gompertz, B. P., Levan, A. J., Tanvir, N. R., et al. 2018, ApJ, 860, 62
Hallinan, G., Corsi, A., Mooley, K. P., et al. 2017, Sci, 358, 1579
Hotokezaka, K., Kiuchi, K., Kyutoku, K., et al. 2013, PhRvD, 87, 024001
Hotokezaka, K., Kiuchi, K., Shibata, M., Nakar, E., & Piran, T. 2018, ApJ, 867, 95
Hu, L., Wu, X., Andreoni, I., et al. 2017, SciBu, 62, 1433
Just, O., Bauswein, A., Pulpillo, R. A., Goriely, S., & Janka, H. T. 2015, MNRAS, 448, 541
Kasen, D., Badnell, N. R., & Barnes, J. 2013, ApJ, 774, 25
Kasen, D., Fernandez, R., & Metzger, B. 2015, MNRAS, 450, 1777
Kasen, D., Metzger, B., Barnes, J., Quataert, E., & Ramirez-Ruiz, E. 2017, Natur, 551, 80
Kasen, D., Thomas, R. C., & Nugent, P. 2006, ApJ, 651, 366
Kasliwal, M. M., Nakar, E., Singer, L. P., et al. 2017, Sci, 358, 1559
Kawaguchi, K., Kyutoku, K., Shibata, M., & Tanaka, M. 2016, ApJ, 825, 52
Kawaguchi, K., Shibata, M., & Tanaka, M. 2018, ApJL, 865, L21

Kilpatrick, C. D., Foley, R. J., Kasen, D., et al. 2017, Sci, 358, 1583
Kiuchi, K., Kawaguchi, K., Kyutoku, K., et al. 2017, PhRvD, 96, 084060
Kiuchi, K., Kyutoku, K., Shibata, M., & Taniguchi, K. 2019, ApJL, 876, L31
Kiuchi, K., Sekiguchi, Y., Shibata, M., & Taniguchi, K. 2009, PhRvD, 80, 064037
Korobkin, O., Rosswog, S., Arcones, A., & Winteler, C. 2012, MNRAS, 426, 1940
Kulkarni, S. R. 2005, arXiv:astro-ph/0510256
Kurucz, R. L., & Bell, B. 1995, Kurucz CD-ROM, Atomic Line List
Kyutoku, K., Ioka, K., Okawa, H., Shibata, M., & Taniguchi, K. 2015, PhRvD, 92, 044028
Kyutoku, K., Kiuchi, K., Sekiguchi, Y., Shibata, M., & Taniguchi, K. 2018, PhRvD, 97, 023009
Lattimer, J. M., & Schramm, D. N. 1974, ApJL, 192, L145
Li, L.-X., & Paczynski, B. 1998, ApJL, 507, L59
Lippuner, J., Fernández, R., Roberts, L. F., et al. 2017, MNRAS, 472, 904
Lippuner, J., & Roberts, L. F. 2015, ApJ, 815, 82
Lipunov, V. M., Gorbovskoy, E., Kornilov, V. G., et al. 2017, ApJL, 850, L1
Lovelace, G., Duez, M. D., Foucart, F., et al. 2013, CQGra, 30, 135004
Margalit, B., & Metzger, B. D. 2017, ApJL, 850, L19
Matsumoto, T., Ioka, K., Kisaka, S., & Nakar, E. 2018, ApJ, 861, 55
McCully, C., Hiramatsu, D., Howell, D. A., et al. 2017, ApJL, 848, L32
Metzger, B. D., & Fernández, R. 2014, MNRAS, 441, 3444
Metzger, B. D., Martinez-Pinedo, G., Darbha, S., et al. 2010, MNRAS, 406, 2650
Metzger, B. D., & Piro, A. L. 2014, MNRAS, 439, 3916
Mooley, K. P., Nakar, E., Hotokezaka, K., et al. 2018, Natur, 554, 207
Nicholl, M., Berger, E., Kasen, D., et al. 2017, ApJL, 848, L18
Perego, A., Radice, D., & Bernuzzi, S. 2017, ApJL, 850, L37
Perego, A., Rosswog, S., Cabezón, R. M., et al. 2014, MNRAS, 443, 3134
Pian, E., D'Avanzo, P., Benetti, S., et al. 2017, Natur, 551, 67
Pozanenko, A., Barkov, M. V., Minaev, P. Y., et al. 2018, ApJL, 852, L30
Radice, D., Galeazzi, F., Lippuner, J., et al. 2016, MNRAS, 460, 3255
Rossi, A., Stratta, G., Maiorano, E., et al. 2019, arXiv:1901.05792
Rosswog, S. 2005, ApJ, 634, 1202
Rosswog, S., Liebendoerfer, M., Thielemann, F. K., et al. 1999, A&A, 341, 499
Rosswog, S., Piran, T., & Nakar, E. 2013, MNRAS, 430, 2585
Ruffert, M., Ruffert, H. T., & Janka, H. T. 2001, A&A, 380, 544
Sekiguchi, Y., Kiuchi, K., Kyutoku, K., & Shibata, M. 2015, PhRvD, 91, 064059
Sekiguchi, Y., Kiuchi, K., Kyutoku, K., Shibata, M., & Taniguchi, K. 2016, PhRvD, 93, 124046
Shappee, B. J., Simon, J. D., Drout, M. R., et al. 2017, Sci, 358, 1574
Shibata, M., Fujibayashi, S., Hotokezaka, K., et al. 2017, PhRvD, 96, 123012
Shibata, M., & Taniguchi, K. 2008, PhRvD, 77, 084015
Shibata, M., Zhou, E., Kiuchi, K., & Fujibayashi, S. 2019, PhRvD, 100, 023015
Siegel, D. M., & Metzger, B. D. 2017, PhRvL, 119, 231102
Smartt, S. J., Chen, T. -W., Jerkstrand, A., et al. 2017, Natur, 551, 75
Tanaka, M., & Hotokezaka, K. 2013, ApJ, 775, 113
Tanaka, M., Kato, D., Gaigalas, G., et al. 2018, ApJ, 852, 109
Tanaka, M., Kato, D., Gaigalas, G., & Kawaguchi, K. 2019, arXiv:1906.08914
Tanaka, M., Utsumi, Y., Mazzali, P. A., et al. 2017, PASJ, 69, 102
Tanvir, N. R., Levan, A. J., González-Fernández, C., et al. 2017, ApJL, 848, L27
Troja, E., Piro, L., van Eerten, H., et al. 2017, Natur, 551, 71
Utsumi, Y., Tanaka, M., Tominaga, N., et al. 2017, PASJ, 69, 101
Valenti, S., Sand, D. J., Yang, S., et al. 2017, ApJL, 848, L24
Villar, V. A., Guillochon, J., Berger, E., et al. 2017, ApJL, 851, L21
Wanajo, S. 2018, ApJ, 868, 65
Wanajo, S., Müller, B., Janka, H.-T., & Heger, A. 2018, ApJ, 852, 40
Wanajo, S., Sekiguchi, Y., Nishimura, N., et al. 2014, ApJL, 789, L39
Waxman, E., Ofek, E. O., Kushnir, D., & Gal-Yam, A. 2018, MNRAS, 481, 3423
Wollaeger, R. T., Fryer, C. L., Fontes, C. J., et al. 2019, ApJ, 880, 22
Wollaeger, R. T., Korobkin, O., Fontes, C. J., et al. 2018, MNRAS, 478, 3298
Wu, M.-R., Fernández, R., Martínez-Pinedo, G., & Metzger, B. D. 2016, MNRAS, 463, 2323